New Insights on the Formation and Breaking Mechanism of Convective Cyclonic Cones in the South Adriatic Pit during Winter 2018

A. PIRRO,[a] E. MAURI,[a] R. GERIN,[a] R. MARTELLUCCI,[a] P. ZUPPELLI,[a] AND P. M. POULAIN[a]

[a] *National Institute of Oceanography and Applied Geophysics (OGS), Sgonico, Italy*

(Manuscript received 24 May 2021, in final form 28 April 2022)

ABSTRACT: The deepwater formation in the northern part of the South Adriatic Pit (Mediterranean Sea) is investigated using a unique oceanographic dataset. In situ data collected by a glider along the Bari–Dubrovnik transect captured the mixing and the spreading/restratification phase of the water column in winter 2018. After a period of about 2 weeks from the beginning of the mixing phase, a homogeneous convective area of ~300-m depth breaks up due to the baroclinic instability process in cyclonic cones made of geostrophically adjusted fluid. The base of these cones is located at the bottom of the mixed layer, and they extend up to the theoretical critical depth Z_c. These cones, with a diameter on the order of internal Rossby radius of deformation (~6 km), populate the ~110-km-wide convective site, develop beneath it, and have a short lifetime of weeks. Later on, the cones extend deeper and intrusion from deep layers makes their inner core denser and colder. These observed features differ from the long-lived cyclonic eddies sampled in other ocean sites and formed at the periphery of the convective area in a postconvection period. So far, to the best of our knowledge, only theoretical studies, laboratory experiments, and model simulations have been able to predict and describe our observations, and no other in situ information has yet been provided.

KEYWORDS: Ocean; Mediterranean Sea; Baroclinic flows; Convective adjustment; Deep convection; Dynamics; Eddies; Mixing; Ocean circulation; Ocean dynamics

1. Introduction

The dense water formation is a critical phenomenon that affects physical, chemical, and biological properties of the water masses at different spatial and temporal scales and is an essential process for the renewal and ventilation of the deep and intermediate ocean water masses. Due to their small scale, intermittent character, and relatively short duration, convective processes are difficult to explore with traditional in situ observations; hence, little is known about their mechanisms and their physical and biogeochemical effects. In addition, considering that any attempt to understand, model, and predict the evolution of the regional/global ocean circulation is influenced by the dense water masses redistribution, a more accurate and detailed assessment of their formation, evolution, and spreading mechanism is mandatory (Testor et al. 2019). The dense water formation process, also called deep convection, composed by the preconditioning, mixing, and spreading phases, occurs only in key regions of the ocean such as the Labrador, central Greenland, and Weddell Seas (Schott et al. 1993; Gordon 1982), and also in the Mediterranean Sea, in particular in the northwestern basin and in the South Adriatic (SA) Sea (Houpert et al. 2016; Cushman-Roisin et al. 2001; Kokkini et al. 2020). The preconditioning phase occurs during early winter in areas with size of 100 km or larger, where the isopycnals doming, induced by the local cyclonic circulation, reduces the stability. The mixing phase takes place when an intense buoyancy loss associated with severe atmospheric conditions erodes the near-surface stratification leading to a large mixed area, the convected area. The spreading phase marks the end of the mixing phase and is responsible for the restratification of the water column.

Using high-resolution glider data collected in the South Adriatic Pit (SAP), a subbasin of the Mediterranean Sea, the present work characterizes in detail the dense water formation process occurring in winter 2018. In particular, the paper focuses on the formation mechanism of *convective cyclonic spinning cones* and their breaking mechanism. These cones develop underneath the convected area during the mixing phase and break within the spreading phase. In situ results are corroborated with reanalysis model products and theoretical arguments.

So far, to the best of our knowledge, the dynamics of these specific types of convective cyclonic cones can only be ascribed to laboratory experiments, numerical analysis, and theoretical arguments (Jones and Marshall 1993; Marshall et al. 1994; Maxworthy and Narimousa 1992, 1994; Visbeck et al. 1996, among others). These studies theoretically explain the physical processes involved with the cones' formation during the mixing phase. That is, when the surface cooling starts to act over the preconditioned area, it produces a three-dimensional (3D) turbulent mixed layer which, unaffected by Earth's rotation, expands from the surface down to a theoretical critical depth Z_c (*convective process*). Below this depth and on a time scale $t \sim O(2\pi/f)$ where f is the Coriolis parameter ($\sim 10^{-4}$ s^{-1} in the SAP), the rotation begins to affect the turbulence and small convective cells called plumes with a horizontal scale ≤ 1 km and vertical velocities up to 10 cm s^{-1} develop (Stommel et al. 1971; Schott and Leaman 1991; Schott et al. 1996; Lilly et al. 1999; Marshall and Schott 1999; Mertens 2000; Margirier et al. 2017). The newly formed plumes, by performing ascending and descending motions, are responsible for "churning" and efficiently mixing the properties of

Corresponding author: Annunziata Pirro, apirro@ogs.it

DOI: 10.1175/JPO-D-21-0108.1

the underneath water column, allowing the convection to penetrate deeper, below the critical depth. This mechanism is responsible for the formation of the mixed layer depth (MLD), which has a horizontal extent of about tens of kilometers (Schott et al. 1993). The plumes that form below Z_c (and within the MLD), come under geostrophic control and a vorticular motion starts to develop in the water column (Legg and Marshall 1993; Maxworthy and Narimousa 1994; Ivey et al. 1995). The above condition can occur only if the ocean depth H is larger than Z_c (for $Z_c < H$); in other words, if the Coriolis effect is prominent (for $R_o^* < 1$), where $R_o^* = Z_c/H$ is the natural Rossby number. In the subsequent days, when the baroclinic instability comes into play (Killworth 1976, 1979; Jones and Marshall 1993), the convective site loses its nearly circular initial shape and breaks up into convective cyclonic spinning cones (*baroclinic adjustment process*). These cones have a theoretical horizontal predictable length scale and extend from the theoretical Z_c down the bottom of the MLD (Nardelli and Salusti 2000). With the continuous deepening of the convective layer, the horizontal density gradient at the edge of the convective region supports the formation of a peripheral rim current in "thermal wind" balance, constraining the convected fluid and the formed cones from further lateral expansion. Once the baroclinic instability is fully developed, this rim current evolves in shape and generates at its edges surface finite-amplitude baroclinic eddies scaled by the Rossby radius of deformation L_ρ.

Fernando et al. (1991) found that for a homogeneous flow, the above theoretical critical depth scales as $Z_c = (B_0/f^3)^{1/2}$, where B_0 indicates the buoyancy flux applied to the region and the natural Rossby number R_o^* introduced above scales as (Jones and Marshall 1993 and Maxworthy and Narimousa 1994)

$$R_o^* = \frac{Z_c}{H} = \frac{B_0^{1/2}}{f^{3/2} H}. \tag{1.1}$$

In the present study, we consider the case of $R_o^* < 1$ ($Z_c < H$), which is a typical condition of the main convection sites, where values of R_o^* range between 0.01 and 1 (Leaman and Schott 1991; Marshall et al. 1994). In addition, considering that the 2018 convection occurs in a stratified fluid, it is more appropriate to describe the vertical evolution of the convective area with the following one-dimensional characteristic depth (Turner 1973):

$$h = \sqrt{\frac{2B_0 t}{N^2}}, \tag{1.2}$$

where N, the Brunt–Väisälä frequency, is a measure of the ambient stratification and the time scale $t \sim O(2\pi/f)$ (Jones and Marshall 1993; Helfrich 1994; Visbeck et al. 1996; Whitehead et al. 1996).

The mixing phase usually ends with the weakening of the atmospheric forcing (Houpert et al. 2016), and the following spreading phase breaks the convective site. However, the end of the convection can also be caused by the submesoscale instabilities developed during the mixing phase and described above (Swart et al. 2015; Thomalla et al. 2015; Du Plessis et al. 2017). The role and the effects of these eddies were first addressed by Killworth (1976, 1979) in his theoretical studies and later by the numerical simulation of Visbeck et al. (1996). These studies show that the newly formed eddies sweep stratified surface waters from outside into the convective region, pushing the convected water downward to greater depths. The established water mass transport sets up a steady state in which lateral buoyancy flux offsets the loss of vertical buoyancy at the surface, thereby arresting the vertical evolution of the MLD. Visbeck et al. (1996), using a "parcel theory," estimated the maximum extension of the MLD, h_{final}, and the time required, t_{final}, to reach it.

The decay of the convection area occurs on a time scale of days (Stommel 1972), and within a week after the end of the cooling, the surface restratification develops on top of the mixed patch (Jones and Marshall 1997). In the present work, the inward stratified water advection (due to lateral eddies) is shown to be responsible for breaking the cones. However, in the event of a new surface cooling, the stratified surface layers may once again be breached, convective plums develop, and the sequence of the events repeated (Jones and Marshall 1993; Houpert et al. 2016).

To support the theory, Maxworthy and Narimousa (1994) simulated in the laboratory the convection process by introducing saltwater only over a limited circular region of a rotating tank filled with homogeneous fluid of depth H. For the case of $Z_c < H$, short-lived vortices formed beneath the source due to the baroclinic instability of the water column. They suggest that the theoretical horizontal scale of the geostrophically adjusted cones is

$$D_{\text{cone}} \sim L_\rho \sim \frac{(B_0^{1/4} f^{1/2} H)^{1/2}}{f} \tag{1.3a}$$

and therefore

$$D_{\text{cone}} \sim \sqrt{R_o^*} H. \tag{1.3b}$$

More precisely, their experiment shows that $D_{\text{cone}} \sim (5.2 \pm 1)\sqrt{R_o^*} H$. However, Phillips (1966) suggests that when the radius of the convective region (r) is greater than h_{final}, a factor of $(r/h_{\text{final}})^{1/3}$ should multiply the original estimate of D_{cone}. The numerical simulations of Jones and Marshall (1993) support the scaling experimentally tested by Maxworthy and Narimousa (1992, 1994) in the laboratory, and the results support each other. Results of a similar laboratory experiment conducted by Marshall et al. (1994) are in agreement with previous works.

In situ data collected in the northwestern Mediterranean Sea during convection periods highlight the presence of cyclonic cones which differ, however, from the ones presented in this study. Using glider data, the comprehensive study of Bosse et al. (2016) examines the physical and dynamical characteristics of deep cyclonic submesoscale coherent vortices (SCVs) formed during the 2009–13 period. These long-lived (~1 year) SCVs with a radius of ~5–8 km seem to be

generated by the bottom-reaching convection and, according to the high-resolution numerical simulations of Damien et al. (2017), they are not linked to the mixing phase. Most likely they are involved in the restratification process when the front bounding the deep mixed patch (~2300 m) becomes baroclinically unstable, allowing the MLD to break. These cyclonic eddies are thus generated around and outside the homogeneous convective area. Evidence of long-lived SCVs have also been observed in other regions like the Labrador Sea convective site (Gascard and Clarke 1983; Lilly and Rhines 2002). The formation process of the above eddies reflects the theoretical and laboratory arguments of a different condition, where $Z_c \geq H$ (or $R_o^* \geq 1$). For this case, the MLD first propagates all the way to the bottom and then spreads radially. After propagating for about one Rossby deformation radius, baroclinic eddies form at the edge and outside the spreading front (and not below the convective site) (Maxworthy and Narimousa 1994; Deardorff 1985).

The SAP, just as other sites of the world, has the prerequisite conditions for an open-ocean convection process (Manca et al. 2002). The presence of the cyclonic SA gyre (Manca and Giorgetti 1998; Kovačević et al. 1999; Poulain 2001; Poulain and Cushman-Roisin 2001) associated with episodes of cold and dry continental air outbreaks (bora wind) enhances the doming structure bringing close to the surface the saline water (mainly the Levantine Intermediate Water) with practical salinity as high as 38.9 (Buljan and Zore-Armanda 1976). This convective site makes the SA the most important source of dense water of the eastern Mediterranean (Pollak 1951; Wüst 1961; Schlitzer et al. 1991; Malanotte-Rizzoli et al. 1997).

In the last decades, numerical studies (Oddo et al. 2005; Mantziafou and Lascaratos 2008; Querin et al. 2013), historical data (Artegiani et al. 1989, 1997), and in situ measurements (Ovchinnikov et al. 1985; Manca et al. 2002; Gačić et al. 2002; Poulain et al. 2012; Kokkini et al. 2020; among others) have been used to investigate the cyclonic circulation of the SA and the dense water formation process. Mantziafou and Lascaratos's (2004) simulations evidence that in the SAP the dense water formation occurs within a small cyclonic eddy ($D \sim 80$ km) located inside the SA gyre ($D \sim 150$ km) having a MLD of ~700 m and the maximum potential density σ_θ of ~29.18 kg m^{-3}. Previous in situ observations confirm that convective MLD ranges between 600 and 800 m with a slightly lower σ_θ between 29.16 and 29.18 kg m^{-3} (Ovchinnikov et al. 1985; Manca and Bregant 1998; Manca et al. 2002; Nardelli and Salusti 2000). However, to the best of our knowledge, no short-lived (order of weeks) cyclonic cones have yet been sampled beneath (and not around/outside) a local homogeneous area, along with their dissipation.

Since 2013, the Mobile Autonomous Oceanographic Systems (MAOS) group of the National Institute of Oceanography and Experimental Geophysics (OGS) has been extensively involved in monitoring the SA deep convection processes using autonomous underwater vehicles. In this work, we use an oceanographic dataset collected by a glider during the Convex 2018 field campaign from 29 January to 17 February 2018 along the Bari–Dubrovnik transect.

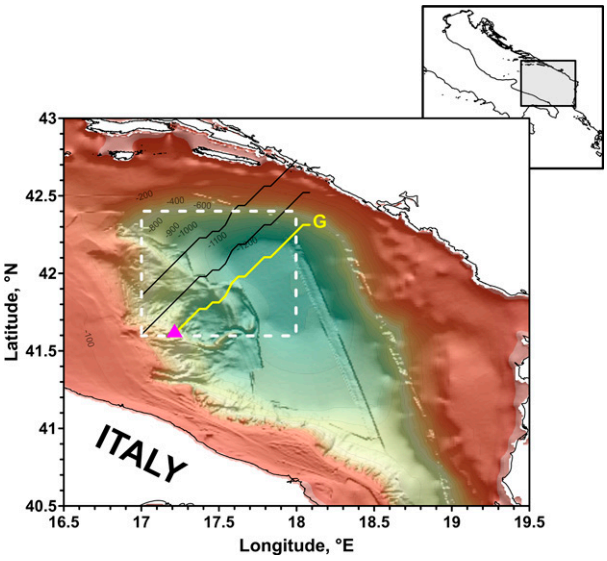

FIG. 1. Bathymetry of the South Adriatic Pit in meters. The white dashed line highlights the study area. The yellow line (G) indicates the modeled Bari–Dubrovnik glider transect closest to the glider trajectory. The latter is calculated by averaging the positions of the first four glider trajectories. Black lines indicate two parallel sections used for inspection, and a magenta triangle indicates the deployment point used to calculate the distances in Figs. 2a–e.

The paper is organized as follows: description of in situ glider data, reanalysis products, and theoretical arguments employed, along with the methods, are described in section 2. Analysis of the glider observations is presented in section 3. The characterization and the dynamics of the modeled convective area is addressed in section 4. Discussion of the results supported by theoretical studies and comparison with modeled reanalysis data are given in section 5. Conclusions and recommendations for future field campaigns are in section 6.

2. Data and methods

a. Glider dataset

The glider data collected during the Convex 2018 field campaign (29 January–17 February 2018) are part of a long project started in 2013 focusing on monitoring the dense water formation in the SAP during the preconditioning period (November–December) and the mixing/spreading phase (January–March). To this end, a Bari–Dubrovnik quasi-zonal transect is conducted twice a year during the winter season. The Convex 2018 mission consists of four repeated ~110-km-long transects (sections 1–4) and an additional truncated transect of about 40 km long (Fig. 1). The Slocum 403 Leonardo glider moved in a sawtooth pattern down to a depth of ~950 m while performing downward and upward profiles. The mean distance between two consecutive surfacings is ~3.5 km and is covered in about 3 h. The glider was equipped with a pumped SeaBird CTD for the measurement of conductivity, temperature, and depth that were sampled at 2-s intervals resulting in

a vertical resolution of about 40 cm (see http://nettuno.ogs.trieste.it/sire/glider/glider_history.php?id_glider_history=34 for the glider technical configuration). CTD data were quality controlled: temperature and salinity data outside the expected range of values in the Adriatic Sea (12°–18°C and 38°–40°C, respectively), and the data corresponding to nonmonotonic pressure values were discarded. Since the mounted CTD was pumped, no thermal-lag correction was applied. Temperature and salinity data were then linearly interpolated over a regular time–depth grid (1 h and 10 m) and over a distance–depth grid (1 km and 10-m depth). The distance was computed from the deployment point (41.6°N, 17.2°E).

Using glider data, the cross-track geostrophic vertical shear was computed by integrating the thermal wind equation for depth–potential density sections 1 and 2, where the most two developed convective cones were sampled. Following the work of Todd et al. (2009), to remove isopycnals oscillations due to internal waves activity, a low-pass filter with a cutoff length equal to the first baroclinic deformation radius was first applied. The modal structure for the first baroclinic mode, performed on a typical density profile, yields a deformation radius of 6 km. Please note that no alterations to the cones' signatures were observed to the filtered profiles. Following a novel method proposed in the work of Bosse et al. (2016), the geostrophic component was computed from the depth average currents (DAC) deduced by the glider and the geostrophic shear (see their appendix A for more details). Specifically, knowing the geostrophic shear $v_g'(r,z)$ [computed as described above) and the total depth-average velocity $v_c(r)$] estimated by the glider, the geostrophic depth-average velocity $\underline{v_g}(r)$ was then retrieved by solving Eq. (A3) in Bosse et al. (2016).

The water vertical velocity w_{water} was inferred by the glider data and computed by following the procedure of Merckelbach et al. (2010), whose methodology is based on a quasi-static flight model. The w_{water} is estimated as the difference between the velocity derived from the rate of change of pressure (z_p, the depth measured by the glider CTD sensor) and that predicted by the optimized glider flight model:

$$w_{\text{water}} = \frac{dz_p}{dt} - w_{\text{glider}}. \tag{2.1}$$

Since we used the same glider hull as in Merckelbach et al. (2010), we adopted some of their flight model parameters. The other parameters specific to our glider hull are listed in Table 1. The drag coefficient (C_{D0}), glider volume (V_g), and hull compressibility (ε) were optimized as required by the method assuming that the mean difference between the observed vertical velocity (derived from pressure sensor output) and the modeled vertical velocity (w_{glider}) is zero for the correct parameter setting. Therefore, by minimizing the cost function [Eq. (16) of Merckelbach et al. 2010] the three parameters were estimated. A recommended window period of 1-day average has been applied. Additionally, only glider data corresponding to an absolute pitch angle higher than 21° were considered to exclude surface or apogee maneuvers.

To estimate the cones diameter from observations we applied Saunders's (1973) theory to the potential density glider measurements (section 3d). He showed that the diameter of a conical feature is $2r_o$, where r_o is the radius of a rotating denser homogeneous water column immersed in a less dense fluid, which slumps under the baroclinic instability. In addition, the DAC estimated by the glider data are also used to estimate the diameter of the cones.

b. *Operational atmospheric and oceanic products*

1) ERA5 ATMOSPHERIC REANALYSIS DATASET

The ERA5 reanalysis operational products were used to compute the surface buoyancy flux (B_0) and the net heat flux (Q_{net}). This dataset combines model data with observations using an assimilation principle based on numerical weather prediction center methods and has a temporal and horizontal resolution of 1 h and 0.25° × 0.25°, respectively. Downward and upward longwave radiation, downward and upward shortwave radiation, latent heat flux, sensible heat flux, total precipitation, and evaporation were considered to compute Q_{net} and B_0. Following Mertens and Schott (1998), B_0 was expressed as

$$B_0 = \frac{g}{\rho_0}\left[\frac{\alpha_\theta}{c_w} Q_{\text{net}} - \rho_0 \beta_s S(E-P)\right], \tag{2.2}$$

where $g = 9.81\ \text{m s}^{-2}$ is the gravity acceleration, $\rho_0 = 1000\ \text{kg m}^{-3}$ is the density reference, $\alpha_\theta = 2 \times 10^{-4}\ \text{K}^{-1}$ and $\beta_s = 7.6 \times 10^{-4}$ are the thermal expansion and the haline contraction coefficients, $c_w = 4000\ \text{J Kg}^{-1}\ \text{K}^{-1}$ is the heat capacity of the water, $E - P$ indicates the net freshwater flux while S represents the sea surface salinity [see section 2b(2) for reference], and Q_{net} is the sum of the four components of the atmospheric forcing: the longwave and shortwave radiation and the latent and sensible heat flux.

2) MEDITERRANEAN SEA PHYSICS ANALYSIS AND FORECAST DATASET

Sea surface salinity used in Eq. (2.2), hourly MLD profiles (based on the σ_θ criterion), and daily maps of seawater

TABLE 1. Parameters of the glider flight, their origin, and values used for Convex 2018. Notation employed follows Merckelbach et al. (2010).

Parameter	Origin	Value
Glider volume (V_g)	Optimized	57.32 L
Parasite drag (C_{D0})	Optimized	0.16 rad^{-2}
Hull compressibility (ε)	Optimized	$1.8 \times 10^{-10}\ \text{Pa}^{-1}$
Reference water temperature (T_0)	Constant (computed)	14.16°C
Glider mass (m_g)	Characteristic of the glider	59.0 kg

potential temperature at the surface and along the glider track, were obtained from Copernicus Analysis Forecast products. They have a horizontal grid resolution of 1/24° (~4 km) and 141 unevenly spaced vertical levels. The potential density (ρ_θ) at different depths was computed from the above temperature and salinity analysis products.

c. Meteorological data

Wind magnitude and direction were collected by the E2-M3A meteorological station, located in the area of the SAP at 41.83°N, 17.75°E (Bensi et al. 2014). The wind data collected 4 m above the surface water with a period of 30 min are obtained by a wind speed and wind direction sensor (Young's Model 04101 Wind Monitor-JR). This instrument has a speed accuracy of ±0.5 m s^{-1} for wind speed less than 10 m s^{-1} and a direction accuracy of ±5°. Collected data are transmitted in real time to an online server by the surface buoy. More details of E2-M3A system can be found at http://nettuno.ogs.trieste.it/eurosites/E2-M3A_SITE.html.

3. Results: Field observations

The Convex 2018 field campaign was performed by the glider from 29 January to 17 February 2018 along the Bari–Dubrovnik transect (yellow line in Fig. 1). This section, as a part of the SAP, is of particular interest for the monitoring of the dense water formation. Specifically, during the winter season this area is subjected to a negative heat flux and the concomitant occurrence of cold and dry bora winds generates vertical and horizontal dense homogeneous regions (e.g., dashed rectangle in Fig. 1) identified as potential areas of convective activity. The formation and the breaking mechanism of the convective cones occurring during this dense water formation process were studied using potential temperature (θ) since this parameter better highlights these features and their evolution. In addition, a list of the parameters employed in the present study is reported in Table 2.

a. Section 1: Bari–Dubrovnik

Potential temperature along section 1 (Bari–Dubrovnik) between 29 January and 1 February is shown in Fig. 2a (middle panel). The 110-km-long transect appears to be highly heterogeneous in space, capturing convective cones at different development stages. Hereafter, the x axis is defined as distance in kilometers from the deployment point.

The first convective cone (named cone A) is centered at ~10 km. This cone in the upper ~400 m of water is delimited by two nearly vertical isotherms (14.23°C) at approximately 5 and 15 km. Its outer boundary is defined by the inward sloped 14.21°C isotherm located at ~150 m of depth while its colder core is defined by the 14.06°–14.16°C lines. The cone potential density (Fig. 2a, lower panel) highlights a dense core ranging between 1029.126 and 1029.15 kg m^{-3} while a near vertical 1029.122 kg m^{-3} isopycnal outcrops at the surface. A water mass with θ = 14.24°C and ρ_θ = 1029.12 kg m^{-3} is also located on both sides of cone A.

Cone B (Fig. 2a, middle panel) is the most evident and well-defined cone; it outcrops at the surface along the 14.14°–14.20°C isotherms between 30 and 40 km and extends down to about 600 m. Its top defined by the 14.06°C isotherm is located at the depth of ~100 m while its core (centered at ~35 km) is colder ($\theta < 14.06$°C) and has a ρ_θ that ranges from 1029.145 to 1029.165 kg m^{-3}. The nearly vertical isotherm of 14.23°C bounds its left side as occurring for cone A. The depth-average currents (Fig. 2a, upper panel) highlight the presence of the cyclonic cone B. The formation of another cone, cone C, at ~60 km pushes the 14.21°–14.25°C isotherms upward letting the 14.19°–14.20°C isotherms (dashed lines in the Fig. 2a, middle panel) be the left and right boundaries of cone C. The rising up of the 14.16°–14.20°C isotherms between 52 and 65 km indicates that cone C is in the process of forming. Other two warm and less dense water patches ($\theta > 14.24$°C, ρ_θ = 1029.12 kg m^{-3}) are found above cone C ($z < 100$ m) and also approximately at 100 km. A homogeneous water column embedded in the 14.19°–14.20°C isotherms (tilted inward) between 70 and 95 km is detected on 1 February. The DAC suggest that the area > 17.8°E is subjected to a cyclonic activity.

Table 2. Parameters used in the present article.

$R_o^* = \frac{Z_c}{H}$	Natural Rossby number
$Z_c = \left(\frac{B_0}{f^3}\right)^{1/2}$	Critical depth
$h = \sqrt{\frac{2B_0 t}{N^2}}$	Characteristic depth for stratified flow
$D_{\text{cone}} \sim \sqrt{R_o^*}\, H$	Theoretical cone diameter
B_0	Buoyancy flux
L_ρ	Rossby radius of deformations
$\text{Ro}_g(r) = v_g(r)/rf$	Geostrophic Rossby number
$g(x, y)$	Cost function
ε	Correction factor
R	Apparent cone radius
$\lvert V_{\max}\rvert$	Mean of peak velocities
R_ε	Corrected apparent cone radius
$V_\varepsilon^{\max}$	Corrected max velocity
$R_o = 2\lvert V_{\max}\rvert/fR$	Rossby number
h_{fin}	Final mixing depth
t_{fin}	Final mixing time
r_o	Radius of the homogeneous water column

b. Section 2: Dubrovnik–Bari

On the way back from Dubrovnik to Bari (from 2 to 6 February), in addition to the formation process of cone C and two other cones (cones D and E centered at ~80 and 100 km, respectively), the glider data also capture the breaking mechanism of cone B (Fig. 2b).

All cones are enclosed within the 14.20°C (1029.128 kg m^{-3}) isotherm (isopycnal). Specifically, on 2 February the 14.14°–14.16°C isotherms rise up to ~250 m, shaping more properly cone E whose outer density is 1029.132 kg m^{-3}. The homogeneous water column detected earlier between 70 and 95 km on 1 February (Fig. 2a) starts to evolve into cone D with a lifting of the 14.16°C isotherm up to ~200 m. The potential density signal follows the potential temperature variations; in particular, the 1029.135–1029.132 kg m^{-3} isopycnals follow the 14.14°–14.16°C isotherms. Therefore, we probably

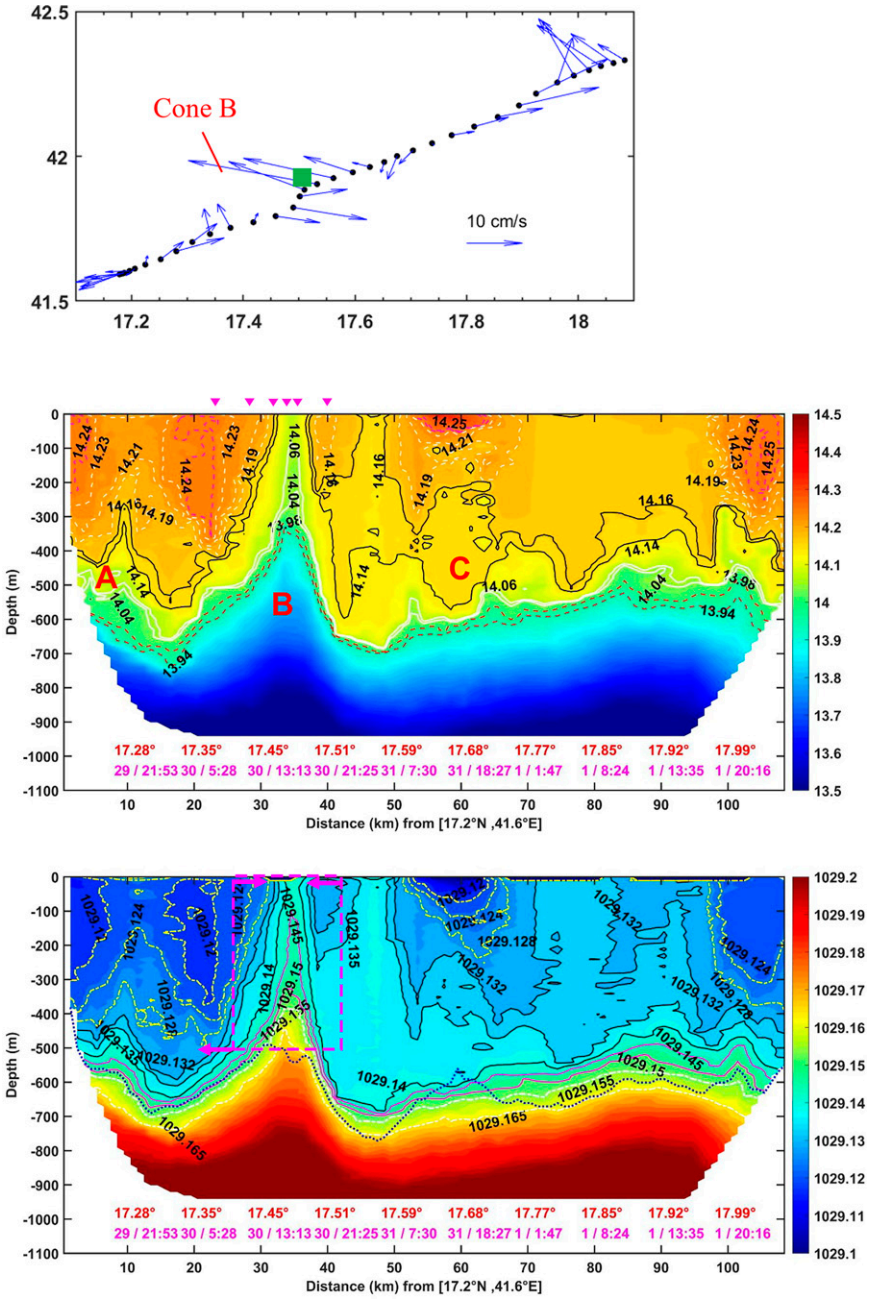

FIG. 2a. (top) Depth-average currents deduced by the glider; the green square indicates the cone B center detected with the cost function. The *x* and *y* axis labels are longitude (°E) and latitude (°N), respectively. (middle) Potential temperature (°C), and (bottom) potential density (kg m^{-3}) measured by the glider along the Bari–Dubrovnik section 1 as a function of depth and distance. On the *x* axis in red is the corresponding longitude (°E) and in magenta the time (days/hours:minutes). From left to right: at ~10 km cone A, at ~30 km cone B, and at ~60 km cone C. Red letters identify the cones, and magenta triangles identify the position of the glider profiles carried out inside the cone B. The dashed box and arrows in the lower panel identify the cone area and the Rossby radius of deformation distance, respectively, used to define the cones diameter. Blue dotted line in the bottom panel show the MLD observed from the glider data.

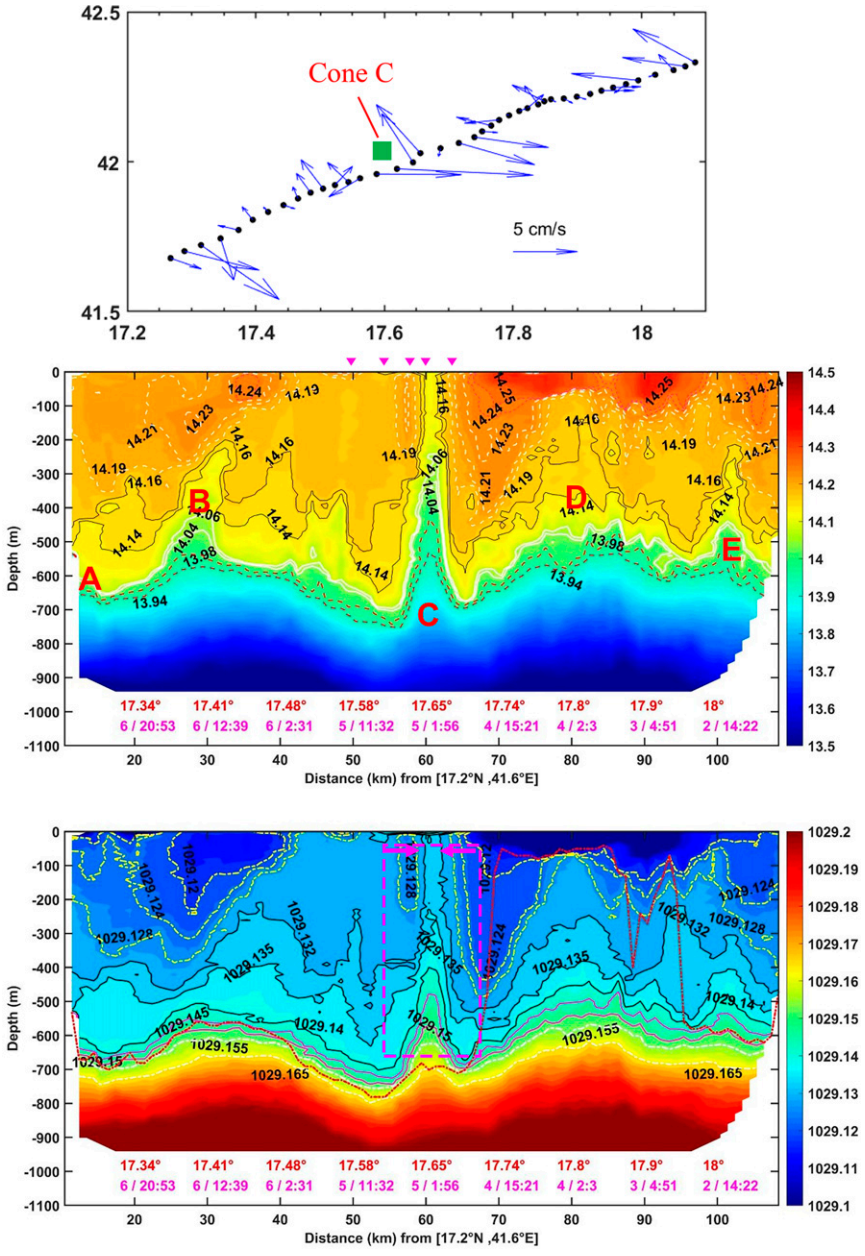

FIG. 2b. (top) Depth-average currents deduced by the glider; green square indicates cone C center detected with the cost function. The *x* and *y* axis labels are longitude (°E) and latitude (°N), respectively. (middle) Potential temperature (°C) and (bottom) potential density (kg m^{-3}) measured by the glider along the Bari–Dubrovnik section 2 as a function of depth and distance. The *x* axis label is the same in as (a). From left to right: at ~30 km cone B, at ~60 km cone C, between 70 and 95 km cone D, and at ~100 km cone E. Red letters identify the cones, and magenta triangles identify the position of the glider profiles carried out inside the cone C. Dashed box and arrows in the bottom panel identify the cone area and the Rossby radius of deformation distance, respectively, used to define the cones diameter. The red dotted line in the bottom panel shows the MLD observed from the glider data.

expect that after a few days, both cones D and E would outcrop at the surface with an isopycnal of 1029.135–1029.132 kg m^{-3}. The DAC at ~17.8° and 18°E still point out a cyclonic activity that most probably can be associated to cone D and cone E. At 60 km, cone C is now fully developed and is similar to cone B (in Fig. 2a, central panel): both 14.14° and 14.16°C isotherms outcrop at the surface while the colder inner core of cone C is defined by the 14.06°C line below the critical depth Z_c. The

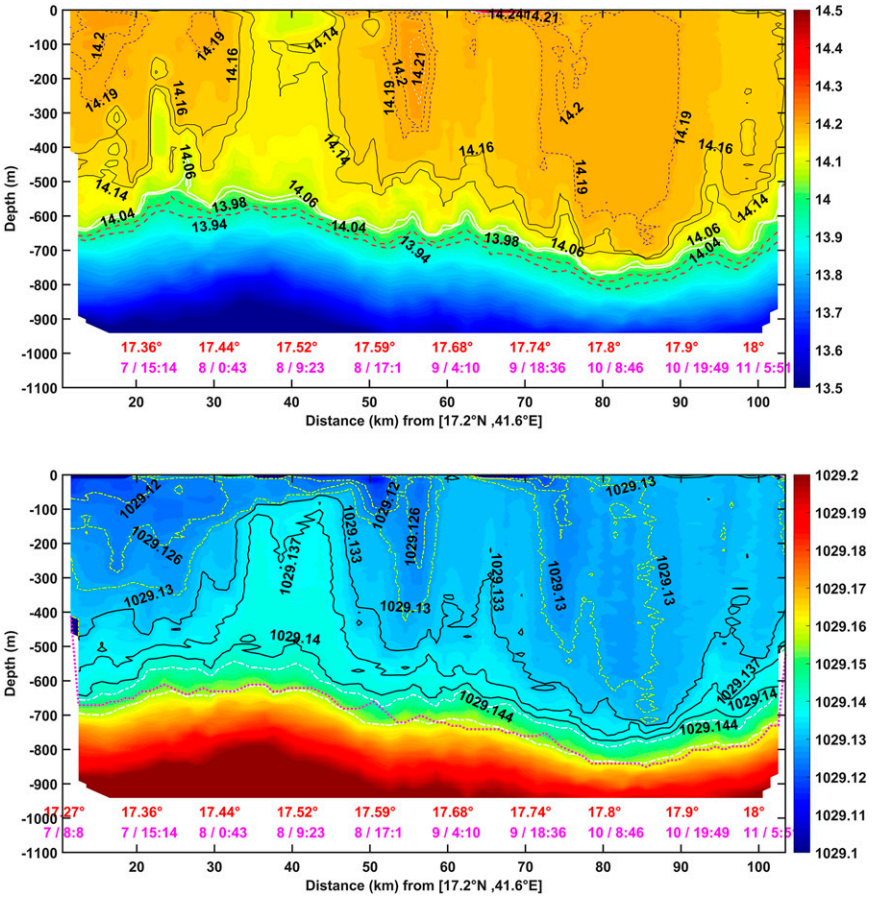

FIG. 2c. (top) Potential temperature (°C) and (bottom) potential density (kg m^{-3}) measured by the glider along the Bari–Dubrovnik section 3 as a function of depth and distance. The *x* axis label is the same as in (a). The magenta dotted line in the bottom panel shows the MLD observed from the glider data.

isopycnal ρ_θ = 1029.132 kg m^{-3} outcrops at the surface while the core of cone C has a ρ_θ larger than 1029.135 kg m^{-3}. Cone C is well detected by the DAC.

By midday on 6 February (Fig. 2b), glider data disclosed a warmer (14.19°–14.24°C) and lighter (ρ_θ < 1029.128 kg m^{-3}) water mass inside the convective area in the upper ~300 m and from the west side (10–40 km). By intruding toward the east, this water mass pushes the upper left side of the cone B, which bends and folds on itself. By late 6 February, residual traces of cone A are present with the 14.04°–14.06°C isotherms reaching the depth of ~650 m (white line in Fig. 2b).

c. *Sections 3–5: Postmixing phase*

From 7 to 11 February along the third Bari–Dubrovnik track (Fig. 2c, upper panel), the 14.04°–14.06°C isotherms that identified cone B and cone C inner core drop between 600 and 700 m, which corresponds to the maximum depth reached by the mixed layer (h_{fin} = 650 m, see section 5) predicted by the theory. Above this depth, patches of 14.19°–14.20°C are embedded within the 14.14°–14.16°C isotherms, except for the area between 35 and 45 km where the 14.14°–14.16°C isotherms still outcrop at the surface.

The in situ potential density (Fig. 2c, lower panel) approximately follows the in situ potential temperature signal, and the range of ρ_θ in the upper 600 m is 1029.12–1029.135 kg m^{-3}, which is larger than 1029.12 kg m^{-3} (water characteristic of the four patches detected in Fig. 2a). The MLD computed from the glider data using the $\Delta\sigma_\theta$ = 0.03 kg m^{-3} criterion, also shows a mixed layer of about 650 m.

Along the fourth Dubrovnik–Bari section (11–14 February) cold (warm) and denser (less dense) patches started to form in the upper 600 m and within the MLD (Fig. 2d, upper and lower panels). This characterization of the water masses becomes more evident on 14–15 February. During this period (fifth section, Fig. 2e upper and lower panel), patches of warmer and less dense water alternate with patches of colder and denser water. Therefore, a sequence of downwelling and upwelling convective cells that probably recall the so-called plumes are detected along the first 40 km, in the upper ~500 m, and for a period of about 27 h.

Following the procedure of Merckelbach et al. (2010), we estimated the water vertical velocity *w* from the glider

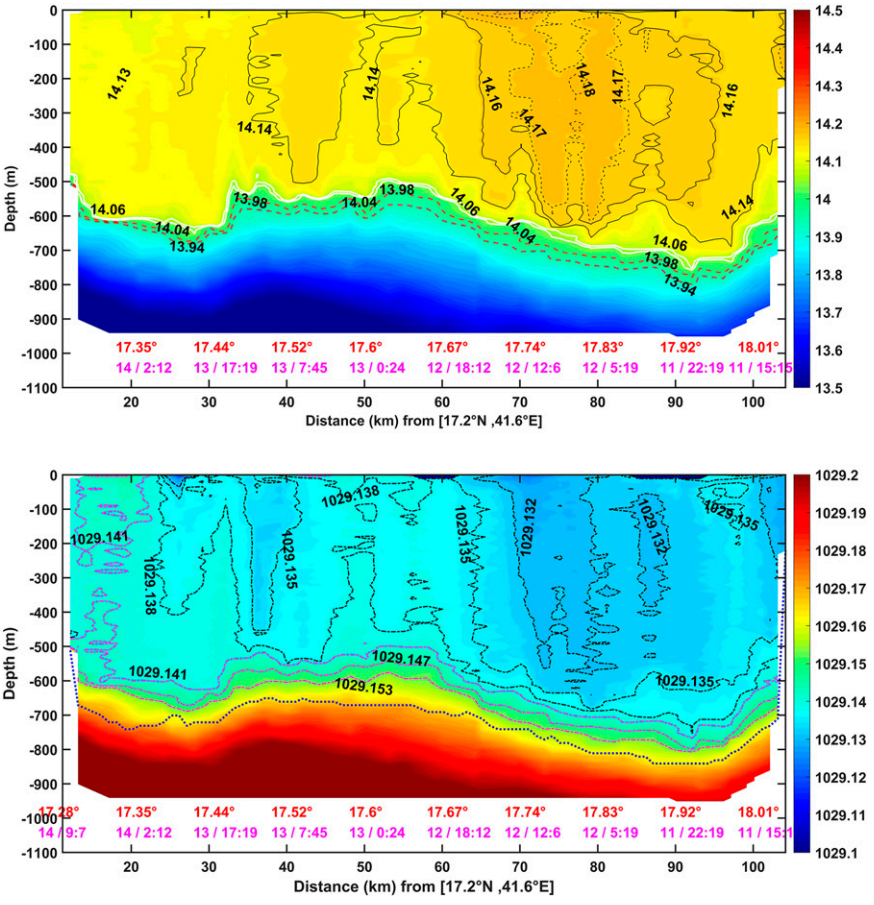

FIG. 2d. (top) Potential temperature (°C) and (bottom) potential density (kg m^{-3}) measured by the glider along the Bari–Dubrovnik section 4 as a function of depth and distance. The x axis label is the same as in (a). The blue dotted line in the bottom panel shows the MLD observed from the glider data.

measurements. From 29 January until ~10 February the velocity w ranged between ± 1.5 cm s^{-1} while an increase of the w in the upper 500 m is registered starting from around 10 February until the end of the campaign (Fig. 3). In particular, between 14 and 16 February, when the sequence of downwelling and upwelling occurs, peaks of ~ -5.5 cm s^{-1} were detected in the upper 500 m.

d. *Cones size characterization*

During the Convex 2018 field campaign, five convective cones along the Bari–Dubrovnik transect were captured by in situ glider observations at different formation stages. Here, we follow the procedure of Saunders (1973) to estimate the diameter of cone B and cone C, which are the most fully developed cones. According to Saunders's theory, a rotating denser water column (e.g., MLD, dashed line in his Fig. 1) surrounded by a less dense fluid slumps to occupy a roughly conical region when the Coriolis effect becomes prominent. Following this mechanism, the surface sides of the MLD slope inward by a distance equal to L_ρ while at the bottom, for the conservation of the angular momentum, the fluid spreads outward by the same quantity L_ρ, as one would expect from the geostrophic adjustment theory (Killworth 1979).

1) CONE B

The observed MLD estimated from the glider dataset identifies the denser water column used in Saunders's theory (and therefore cone B) in the upper ~550 m. The horizontal extension of this denser water column, which most probably evolved into cone B, was reconstructed backward. That is, at the surface, on both sides of cone B and from the inward sloping isopycnal (ρ_θ = 1029.132 kg m^{-3}), a distance of $L_\rho \sim 6$ km is drawn and highlighted by two arrows pointing inward (Fig. 2a, lower panel). The end of each arrow defines thus the right and left boundary of the water column (magenta dashed line), which in turn results to have a horizontal extension that goes from 17.39° to 17.53°E.

To conclude, according to Saunders (1973), at the surface the isotherms and/or isopycnals slump inward by a distance equal to L_ρ. At the bottom left ($z \sim 550$ m), the 1029.132 kg m^{-3} isopycnal slopes outward by the same distance L_ρ, while on

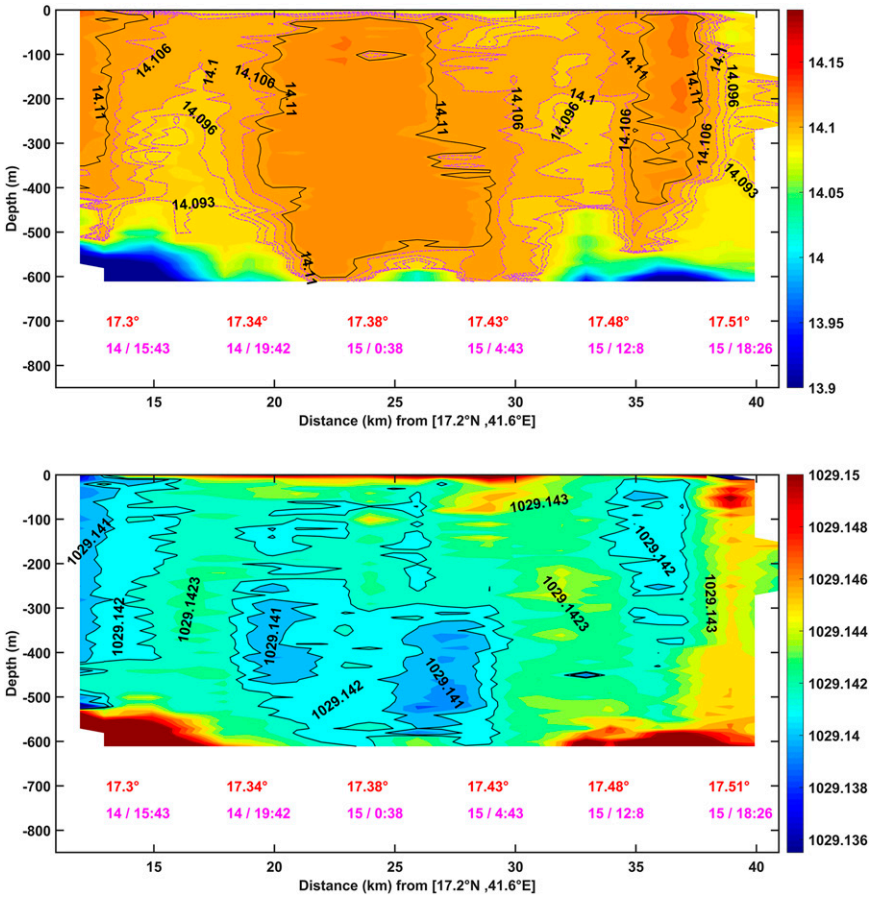

FIG. 2e. (top) Potential temperature (°C) and (bottom) potential density (kg m^{-3}) measured by the glider along the Bari–Dubrovnik section 5 as a function of depth and distance. The *x* axis label is the same as in (a).

the right side this mechanism is not observed. With regard to this, we have to make three considerations. First, cone B is not isolated and the interaction with lateral cones could affect its dynamics; second, a further evolution of cone B could be possible in the subsequent days; third, we are not completely certain that the glider crossed exactly the center of the cone B (see section 3e). Therefore, from the in situ observations, cone B has a maximum diameter of ~13 km and a center close to 17.48°E.

2) CONE C

Based on the observed MLD, the denser water column for cone C is defined approximately in the upper 650 m. As done for cone B, the spatial extension of the corresponding water column was reconstructed backward (Fig. 2b, lower panel). At the surface, the arrows confirm that the isotherms and/or isopycnals slump inward by the same quantity ($L_\rho \sim 6$ km). Near ~650 m, the outward sloping is not present, probably for the same considerations valid for cone B. The detected water column highlighted by the magenta dashed line thus extends between ~17.61° and 17.71°E. Therefore, from the in situ observations the maximum diameter of cone C is ~10 km and its center close to 17.67°E.

e. *Cones center detection and cyclostrophic velocities*

To better characterize the most two developed cones (cone B and C), we followed the procedure adopted by Bosse et al. (2015, 2016) to infer the cyclostrophic velocities and the cones center. To estimate the velocity field within eddies characterized by strong horizontal shear ($>0.1f$), it is important to consider the nonlinear effect (e.g., the centrifugal force); otherwise, its neglection would result in an overestimation of the velocities in the cyclonic eddies and an underestimation in the anticyclonic eddies (Elliott and Sanford 1986; Penven et al. 2014; Bosse et al. 2015). To this end, the cyclostrophic velocities v_c can be computed by solving the quadratic gradient wind equation in a cylindrical coordinate system:

$$\frac{v_c^2}{r} + f v_c = + f v_g, \tag{3.1}$$

where r is the distance to the cone center, f is the Coriolis parameter, and v_g is the geostrophic velocity (method

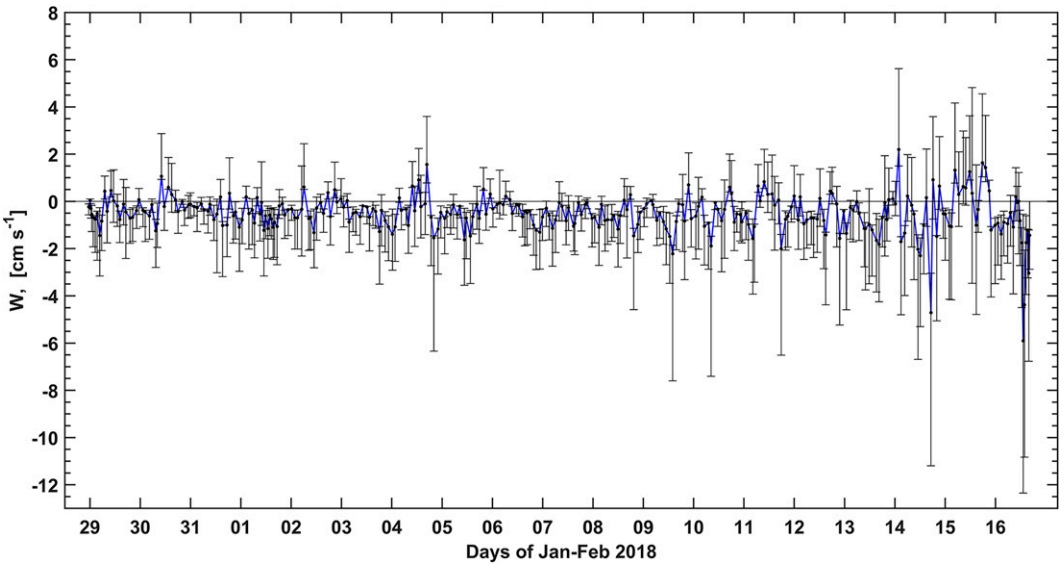

FIG. 3. Vertical currents in the upper 500 m estimated from glider measurements using Merckelbach et al. (2010) procedure. Black bars indicate the 10th–90th percentile range.

described in section 2a). To solve this equation, the remaining unknown (the distance r to the cone center) is estimated from the depth-average currents and described below. By solving analytically for v_c [Eq. (3.1)] and keeping only the "normal" solution (which corresponds to the positive sign), it yields

$$v_c(r) = \frac{rf}{2} \times \left[-1 + \sqrt{1 + 4\frac{v_g(r)}{rf}} \right], \tag{3.2}$$

and therefore, the geostrophic Rossby number is defined as $\mathrm{Ro}_g(r) = v_g(r)/rf$. Considering that for our case of study $\mathrm{Ro}_g(r)$ is positive and varies between 0.2 and 0.28, and that Eq. (3.2) can be approximated (using Taylor expansion) to $v_c(r) \cong v_g(r)[1 - \mathrm{Ro}_g(r) + 2\mathrm{Ro}_g(r)^2 \cdots]$, as expected, the cyclostrophic velocities are smaller in magnitude than the geostrophic one. A correction factor of about 12% hence needs to be taken into account.

To estimate the position in space of the center of cones B and C with respect to the glider path, as done in Bosse et al. (2015), we adopted a procedure that uses the depth-average currents estimated by the glider minus a mean advection. The latter, for this study, is defined by averaging the DAC within a running window of ~±1 day and ±25 km, which accounts for the large-scale circulation features. To this end, the following cost function g was minimized:

$$g(x, y) = \frac{1}{n} \sum_{i=1}^{n} \left[v_i \frac{r_i(x, y)}{\|r_i(x, y)\|} \right]^2, \tag{3.3}$$

where v_i is the dive average velocity estimated by the glider (minus the mean advection) at a given position (x_i, y_i) in the horizontal plane and $r_i(x, y)$ is the vector from (x, y) to (x_i, y_i). This method was applied to both cones B and C and, to keep the measurements as synoptic as possible, we chose at most $n = 5$ centered around each cone. This corresponds to a temporal window of about 10 h. The minimization of the cost function g provides the position of the cone's center in the horizontal plane and ensures that the direction of the cone center position (x_i, y_i) is the most perpendicular to the depth-average currents. Figure 4 shows the cost function and the center position (magenta star) for cones B and C. Since for both cases the glider did not cross exactly the center, a factor $\varepsilon = \sqrt{1 + d^2/R^2}$ with d the distance between the glider section and the estimated cone center and R the apparent radius (defined as half radial distance between the two opposite peak velocities), was considered and applied to the apparent cone radius and velocities such as $R_\varepsilon = \varepsilon R$ and $V_\varepsilon^{\max} = \varepsilon V_{\max}$, where $|V_{\max}|$ is the mean of the peak velocities. Note that ε is near 1, and specifically equal to 1.003 (1.04) for cone B (cone C), while $V_{\max}$ is 16 cm s^{-1} (10 cm s^{-1}) for cone B (cone C). The Rossby number defined as $R_o = \nabla \times v_h/f$ (with $\nabla \times$ the curl operator and v_h the horizontal currents), is here approximated by $2|V_{\max}|/fR$ for the case of circular vortices in solid body rotation. For cone B (cone C) R_o is 0.4 ± 0.12 (0.36 ± 0.11), and these values confirm that nonlinear terms are relatively important in the dynamical balance of both cones.

4. Modeled dynamics of the convective site

High-resolution glider measurements are of paramount importance for the detection and the characterization of the convective cones. However, to overcome their spatiotemporal limitation, reanalysis products were used to identify and study the dynamics of the area (hereafter called study area) encompassing the cones described previously. To this end, based on modeled temperature, a vertically and horizontally

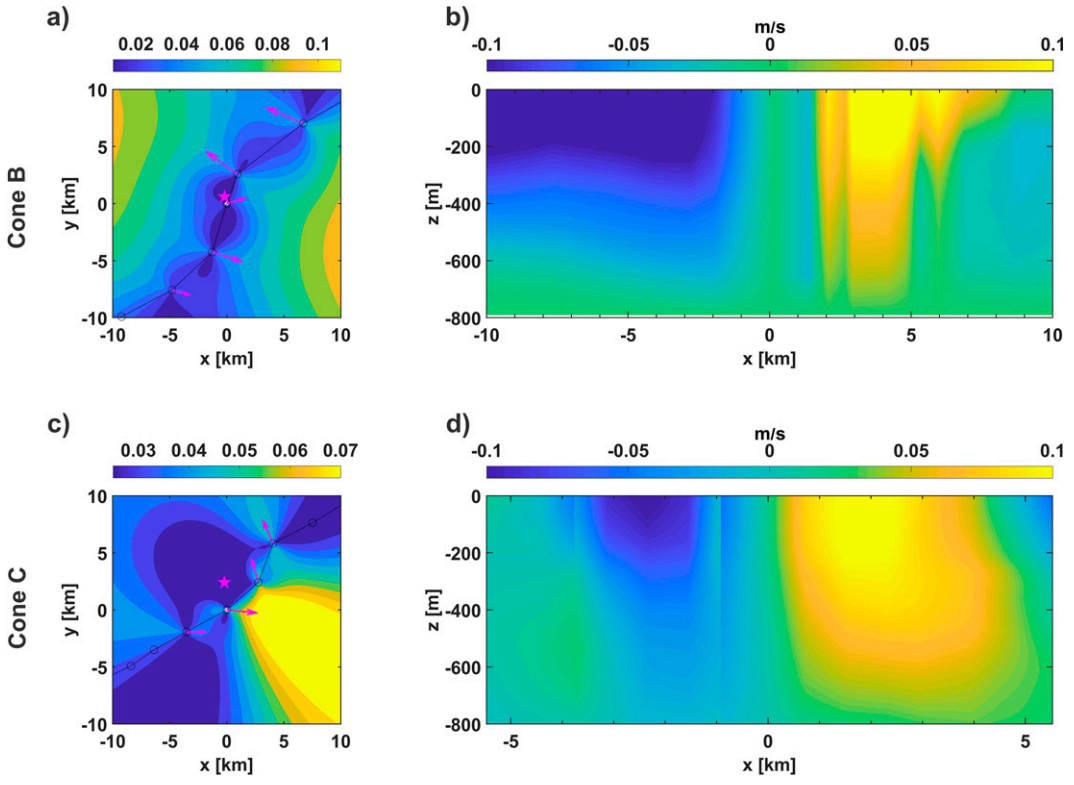

FIG. 4. (a),(c) Cost function used to detect the center of the cones (magenta star) along with depth-average currents (minus the mean advection) deduced by the glider, and cyclostrophic velocities cross section, respectively, for (b) cone B and (d) cone C. Black circles in (a) and (c) indicate the position of glider profiles.

homogeneous region of a nearly circular shape was detected within ~17°–18°E, 41.6°–42.4°N (dashed rectangle in Fig. 1). In addition, this study area along with the whole SAP is subject to a negative heat flux (~−200 W m^{-2}, not shown) and therefore is identified as a potential area of convective activity.

Figures 5a and 5b show the evolution of the hourly MLD and of the potential density (both averaged over the study area) at different depths from 30 to 700 m. Starting from about 11 January, the model indicates a deepening of the MLD, in accordance with the gradual increase of potential density, from 30 m down to 600 m. This behavior indicates that the mixing phase is in place and its beginning (~11 January) coincides with the increase of the negative buoyancy flux (Fig. 5c) that reaches its maximum (-1.1×10^{-7} m^2 s^{-3}) between 14 and 25 January. This period is not fully associated with intense and continuous northerly bora winds; however, some wind bursts (~15 m s^{-1}) occurred therein on both 17 and 22 January (Figs. 5d,e). As a consequence, on 17 January a sharp increase of ρ_θ is evident in the upper 100 m (Fig. 5b) as well as the deepening of the MLD during both wind events. On 24 January the MLD reaches about 400 m, and in conjunction with a northerly wind burst occurring on 28 January, the MLD further deepens down to ~550 m. The ρ_θ sharply increases within the 30–600 m layers, and a maximum of $\rho_\theta = 1029.16$ kg m^{-3} is reached. From ~29 January to approximately 5–6 February, the 30–600 m layer has an averaged $\rho_\theta \sim 1029.15$ kg m^3. Afterward, the ρ_θ starts to decrease corresponding to the end of the mixing event. From ~10 February until 17 February, the increasing (deepening) of the ρ_θ (MLD) suggests that a second mixing event is in place.

The dynamics of the study area is investigated using maps of modeled temperature at the surface and along the glider section (Fig. 6). At the beginning of the mixing phase (~10–11 January) the surface warm (>15.5°C) SA gyre is displayed in Fig. 6a and, within it, two subregions of 14.55°–14.60°C are highlighted by cyan isotherms approximately located north (>41.8°N) and south (<41.8°N) of the yellow glider track (Fig. 6a). A signature of colder surface water (<14.45°C, red isotherm) is more pronounced south of 41.6°N. Along the vertical glider section, the stratification is evident; however, a well-developed doming is shown at the western edge of the transect and in the upper 80–400 m, while a less pronounced one is present between 17.7° and 17.9°E (Fig. 6b). With the progression of the mixing phase, the surface study area becomes colder and the MLD along the glider section increases. By 23 January, a day after the wind burst occurred, four mixed patches developed along the glider transect and in the upper 200–300 m (Fig. 6d). That is, two 300-m-deep homogeneous areas (14.36°C) are displayed above the first doming (early detected at ~17.3°E) and at ~17.5°E while a shallower ($z \sim 200$ m) homogeneous area (14.44°C) forms above the second doming (previously

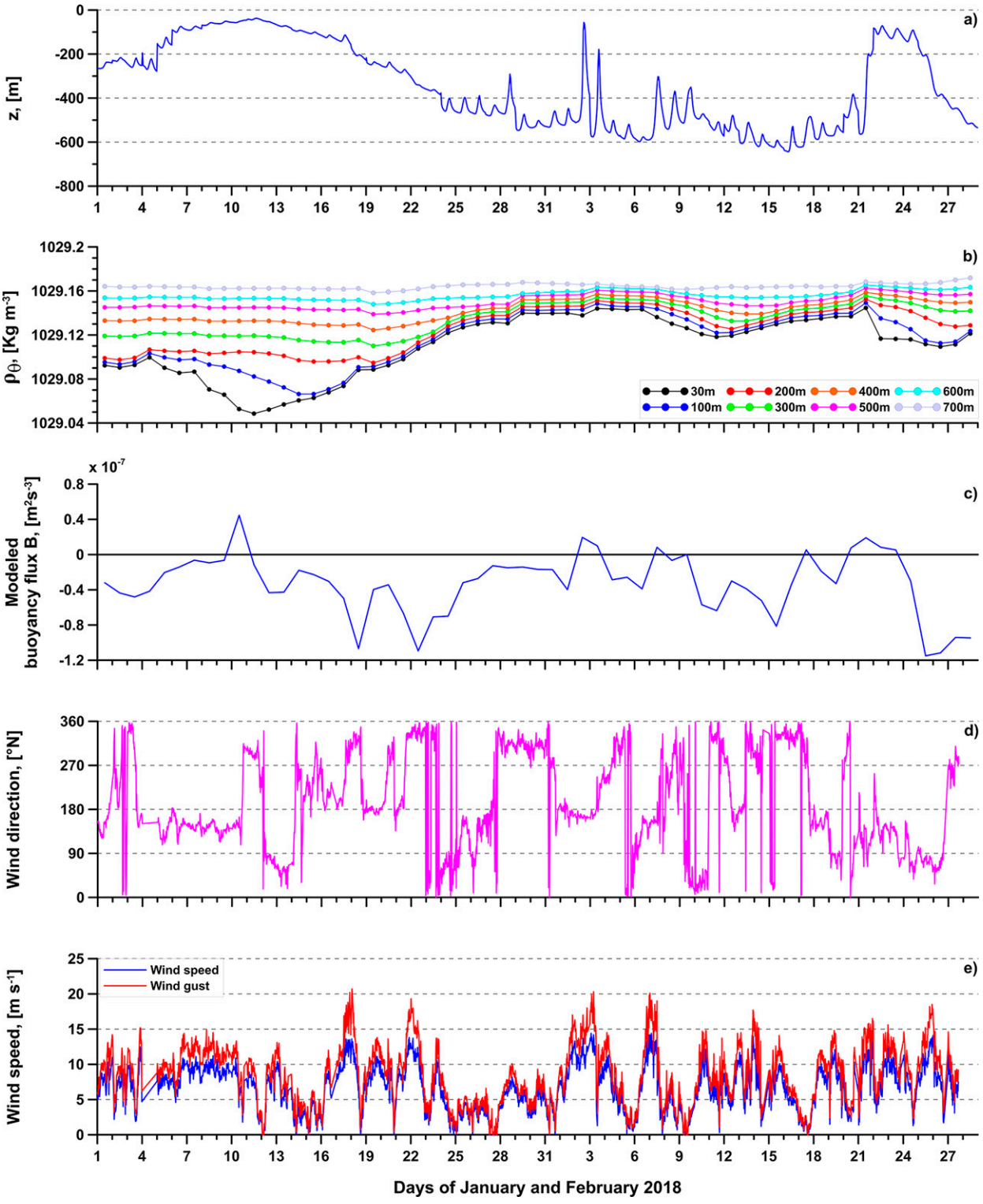

FIG. 5. (a) Hourly modeled MLD averaged for the study area, (b) modeled potential density at different depths averaged for the study area, (c) modeled buoyancy flux B averaged for the study area, (d) wind direction, and (e) speed collected at the E2-M3A buoy.

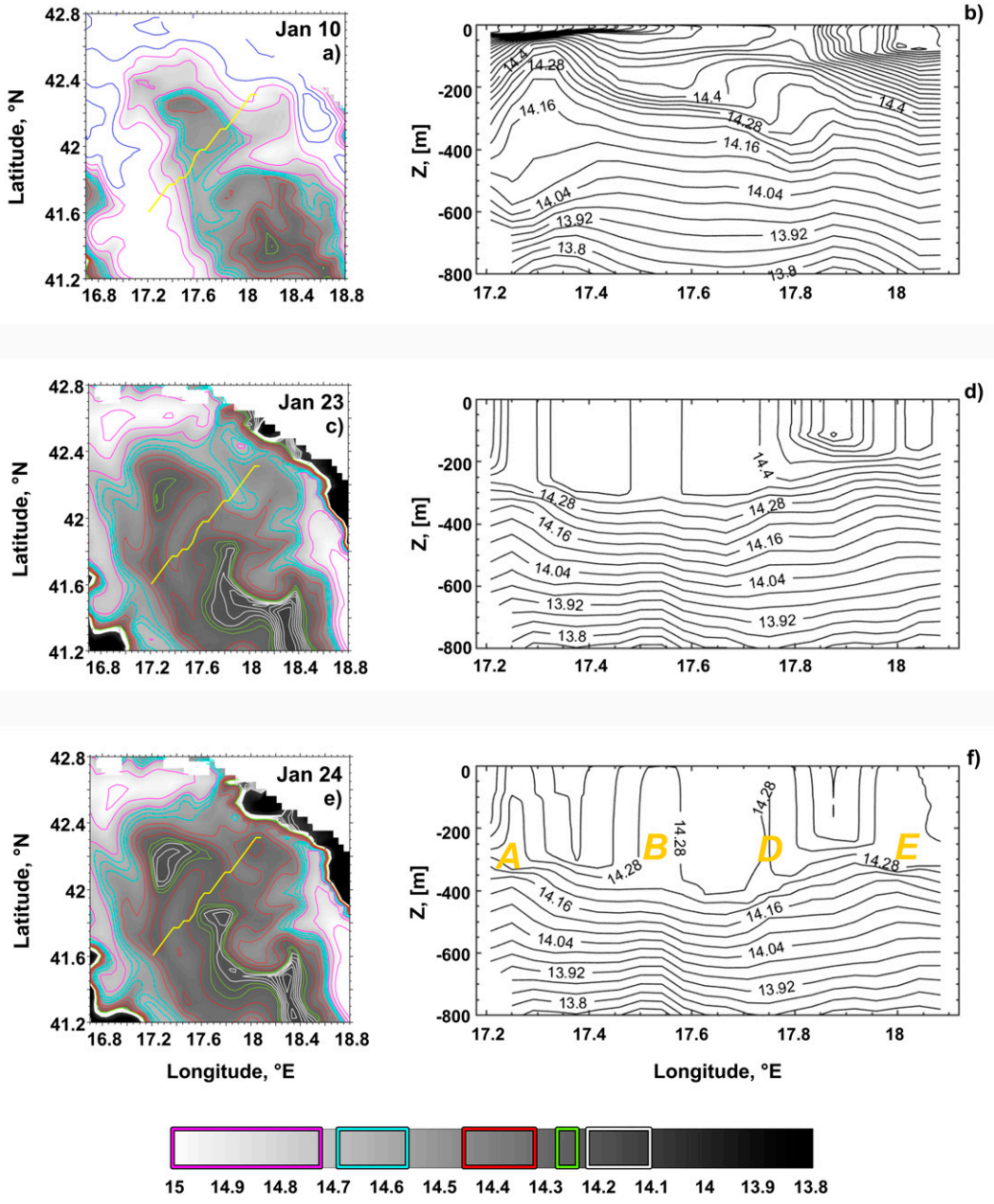

FIG. 6. (left) Daily reanalysis seawater potential temperature maps. Colored lines indicate different isotherms. That is, white (14.1°–14.22°C), green (14.24°–14.26°C), red (14.31°–14.45°C), cyan (14.55°–14.69°C), magenta (14.7°–15°C), and blue (15.2°–15.6°C). Glider track (G) is in yellow. (right) Depth–longitude reanalysis potential temperature along the glider track G. Yellow letters indicate the cones. Color bar units are in °C, and colored blocks highlight different isotherm intervals.

described) and also at 18°E. At the surface, the study area is visibly colder ($\theta < 14.55$°C) and an even colder localized patch (~14.26°C) is present at ~42.1°N (Fig. 6c). South of 41.8°N, the red gyre which encloses the coldest water (white isotherms) and recalls the inner gyre, predicted by Mantziafou and Lascaratos (2004), exhibits a mushroom-like feature along its eastern flank (~41.6°N). This feature is typical of baroclinic instability (Blokhina and Afanasyev 2003), and it is better shaped at the surface on 24 January (Fig. 6e). On the same day, the vertical homogeneous water columns previously formed on 23 January evolve in shape as a consequence of baroclinic instability (Fig. 6f). Specifically, both sides of each MLD slope inward and a total of four cones (cone A, cone B, cone D, cone E) start to develop within the14.63°C isotherm (Fig. 6f).

For a more comprehensive analysis of the study area, modeled temperature along two parallel transects (black

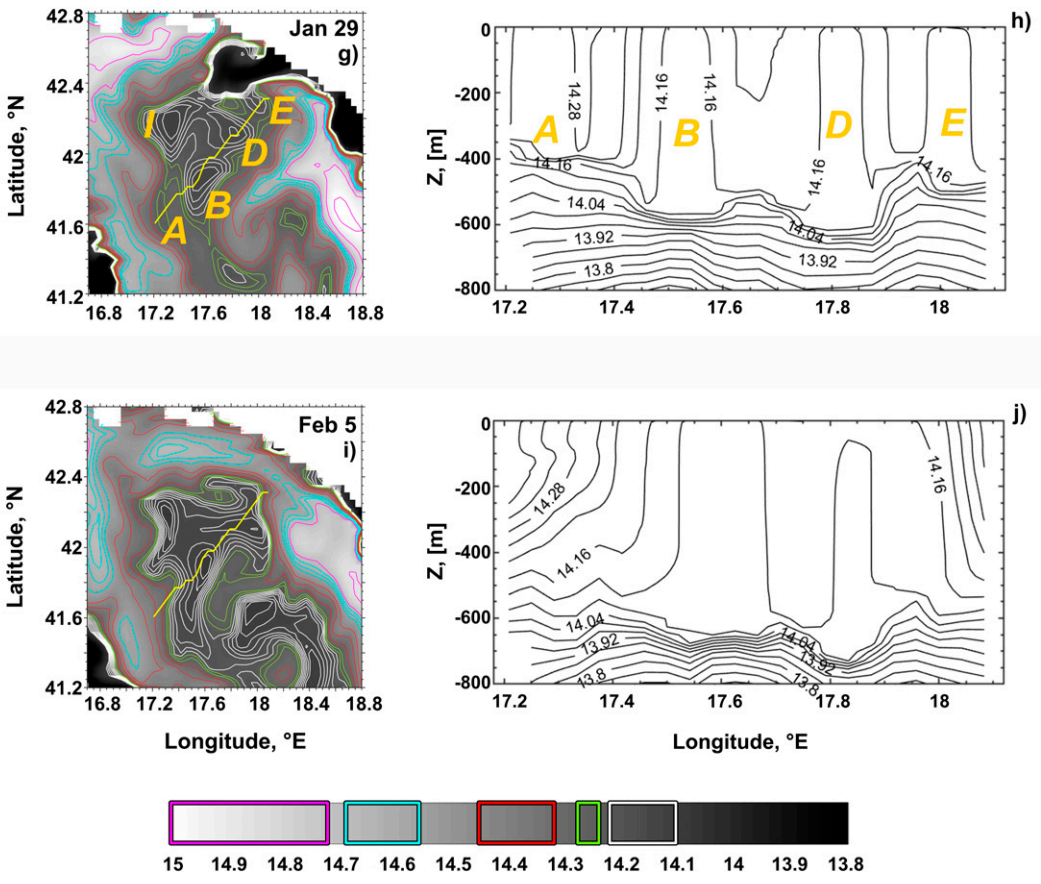

FIG. 6. (*Continued*)

lines in Fig. 1) were also considered. However, since they exhibited the same temporal evolution of the modeled section along the glider transect, they are not shown here. Nevertheless, it is important to point out that cone I formed approximately at 42.1°N within the cold area (14.1°–14.26°C, Fig. 6e).

On 29 January, 5 days later (Fig. 6g), a near circular homogeneous horizontal area highlighted by the green 14.24°C isotherm occupies the whole study area, and the signature of the convective cones B, D, E, and I is displayed within it. Cone A, identified at ~17.3°E on 24 January (Fig. 6f), probably corresponds to the small surface patch (14.26°C) highlighted at the same longitude on 29 January (Fig. 6g). Cone A vertical signature (Fig. 6h) is defined by the 14.28°C isotherm while, cone B outcrops at the surface with the 14.16°–14.20°C isotherms, in the upper 500 m, and between 17.45° and 17.61°E.

Cone D, simulated by the model, is defined by the 14.16°C isotherm at approximately 17.8°E (Fig. 6h) and is embedded within a warmer area (~14.20°C).

Last, cone E, located at the easternmost part of glider transect (~18°E), is simulated by the model on 29 January and is defined by the 14.2°C isotherm (Fig. 6h).

By 5 February, which approximately coincides with the end of the mixing phase as indicated by the potential density decreasing (Fig. 5b), the surface shape of the convective site (white and green isotherms in Fig. 6i) evolves in a way that recalls the evolution of a convective area constrained by a rim current under baroclinic instability (Visbeck et al. 1996, their Fig. 2) and 4–5 meanders with a wavelength $L \sim 25$–30 km surround the surface homogenous convective site. A warm lateral intrusion in the upper 400 m and at the western side of the glider transect (Fig. 6j) is evident on 5 February and becomes more pronounced the following days.

The reanalysis model data were used to reconstruct (before and after the glider measurements) the dynamics of the study area enclosing the cones. After a period of approximately 2 weeks from the beginning of the mixing phase (~10–11 January) the baroclinic instability affects the study area. That is, on 24 January a ~300-m-deep convective site with $\theta \sim 14.24°C$ and $\rho_\theta \sim 1029.122$–$1029.13$ kg m^{-3} (Figs. 6f and 5b) breaks down into convective cones. These cones do not substantially migrate from their initial position; however, during the entire mixing phase period they become colder and are always constrained within the convection region, which is approximately 100 km wide. Lateral intrusion of stratified water is responsible for their collapse.

5. Discussion and considerations

The observations presented in section 3 complemented with reanalysis products discussed in section 4 allow us to make the following considerations that explain in detail the mixing and spreading/restratification phase dynamics of the convection process in the SAP during winter 2018. Specifically, the formation process, the characterization and the breaking mechanism of cyclonic convective cones constitute the main interest of the present work.

The homogeneous convective site identified as the study area and characterized by $\theta \sim 14.24$°C and $\rho_\theta \sim 1029.122$–$1029.13$ kg m^{-3} experiences a mixing event approximately from 11 January until 5–6 February (Figs. 5a,b) by reaching a maximum theoretical mixing depth $h_{\text{fin}} \sim 650$ m [see Eq. (5.1) for details]. The deepening of the MLD on ~11 January (Fig. 5a) marks the beginning of the *convective* process (although no trace of plumes is detected due to the low horizontal resolution of the reanalysis model, and the scarcity of in situ measurements), while the *baroclinic adjustment* process sets in almost simultaneously on a time scale of $t \sim O(2\pi/f)$ ~1 day [in compliance with the theoretical prediction of Legg et al. (1998)]. As time elapses, the instability grows and a mushroom and later on, a hook-like feature forms along the cyclonic inner gyre on 23 January (Figs. 6c,e,f). Afterward, when the baroclinic instability is fully developed, the available potential energy accumulated within the dense-water convective site is released, and at its periphery the instabilities emerge as meanders. To this end, on 29 January 4–5 meanders highlighted by the green-white isotherms surround the dense homogenous convective site (Fig. 6g). These meanders have a wavelength $L = 2\pi L_\rho \sim 25$–30 km with $L_\rho = Nh_{\text{fin}}/f \sim 6$ km (being $h_{\text{fin}} \sim 650$ m, $N \sim 10^{-3}$ s^{-1}, and $f = 10^{-4}$ s^{-1}). Similar values of L_ρ and L were found by Grilli and Pinardi (1998) and by Mantziafou and Lascaratos (2004), respectively.

Following Eady (1949), we estimate the instability growth rate (s^{-1}) of the baroclinic disturbance:

$$\sigma \sim \frac{f}{\sqrt{\text{Ri}}} \sim \frac{f\,\dfrac{\partial u}{\partial z}}{N}, \tag{5.1}$$

where Ri is the Richardson number, and the vertical shear of the zonal velocity and the frequency N were computed from the potential temperature and salinity data collected by the glider. Along the Bari–Dubrovnik section 1, σ (not shown) values reveal that the time for baroclinic instability to develop is on the order of 2 weeks. Therefore, this result proves that from the beginning of the mixing event and within a time period on the order of 2 weeks, the convective site undergoes the baroclinic instability process which, consequently, leads to the formation of cyclonic cones in the study area. (Figs. 2a and 6e,f,g,h).

An additional proof that the convective process proceeds through the development of cones of geostrophically adjusted fluid is also supported by the fact that the historical data in the SAP have never recorded a MLD greater than ~800 m (Manca and Bregant 1998; Manca et al. 2002; Nardelli and Salusti 2000, among others) and therefore, the condition $Z_c < H$ (1200 m) is met. Specifically, to reach a MLD greater than the SAP bottom depth (h = 1200 m), the SAP should experience a continuous constant buoyancy flux $B_0 = 10^{-7}$ m^2 s^{-3} ($Q_{\text{net}} \sim 300$ W m^{-2}, which is the maximum value registered in January 2018) for a time $t \sim 3$ months [Eq. (1.2)]. Clearly, these conditions are not met during winter 2018.

Five convective cones (cone A, cone B, cone C, cone D, cone E) were thus detected by the glider along the Bari–Dubrovnik transect from 29 January to 6 February 2018, and reanalysis data suggest that they develop inside the ~110-km-wide convective region and within vertical homogeneous water columns a day after these columns are fully developed (Figs. 6c–f). The time of cones appearance is in agreement with Saunders's (1973) theory, which argues that after a time $t \sim O(2\pi/f)$ (~1 day) from the homogeneous water column formation, the fluid starts to evolve into a conical shape. In agreement with theoretical analysis and laboratory experiments (Maxworthy and Narimousa 1994), cone A (Fig. 2a) forms below the critical depth $h \sim 100$ m [Eq. (1.2) with $t \sim O(2\pi/f) \sim 1$ day, $N^2 \sim 10^{-6}$ s^{-2}, $B_0 \sim -0.6\ 10^{-7}$ m^2 s^{-3}] where the fluid adjusts toward the geostrophic balance and forms the cone features by tilting inward its isotherms/isopycnals. The in situ patches with $\theta \geq 14.24$°C and ρ_θ of 1029.12 kg m^{-3} located at both sides of cone A (Fig. 2a) are a reminiscence of the MLD that early developed, and later was broken down into the cone A. Two other patches with the same characteristic were detected by the glider at distances of 60 and 100 km. Reanalysis potential temperature confirms that cones develop within the 14.24°C isotherm (17.4°–18.1°E, Fig. 6h).

Although both modeled and in situ cone B outcrop at the surface with the same isotherms (14.14°–14.16°C), the modeled one is slightly shifted to the east (Figs. 6h and 2a). In addition, high-resolution glider data are able to resolve the colder core (≤14.06°C) of cone B while model outputs cannot. The DAC along the section confirm the presence of the cyclonic cone B. As for cone A, also cone B forms in the layer below the critical depth where Coriolis effect is prominent.

According to the above literature, when the conditions for cones formation are met, a homogeneous water column could break down into one or more cones. Here, the homogeneous area (~14.20°C/1029.128 kg m^{-3}) identified on 1 February between 70 and 95 km and in the upper ~400 m (Fig. 2a) could follow this mechanism, and the lifting of the in situ 14.16°C isotherm ($z \sim 350$ m, Fig. 2b) is therefore the prelude to cone D and cone E formation. A cyclonic activity highlighted by the DAC east of 17.8°E along both sections 1 and 2 confirms this hypothesis.

Cone D simulated by reanalysis data is defined on 29 January by the 14.16°C isotherm at approximately 17.8°E (Fig. 6h), and it is embedded within a warmer area (~14.20°C). However, we observe that modeled data anticipate its formation since, from in situ glider data (Fig. 2a, central panel), the large homogeneous area of 14.20°C is still present at the same longitude (17.8°E) on 1 February, and no signature of cone D is yet sampled.

Last, cone E, located at the easternmost portion of the glider transect (~18°E), is simulated by temperature reanalysis data on 29 January and is defined by the 14.2°C isotherm (Fig. 6h), while in situ potential temperature shows that the 14.14°–14.16°C isotherms are still rising on 1 February and cone E will form on 2 February (Figs. 2a,b).

Although a comparison between reanalysis and in situ data was possible for cones A, B, D, and E, no information is given on cone C, which was only captured by in situ glider data. Probably, the shifting to the east of cone B in modeled output is the reason for cone C's absence. In light of the discrepancies highlighted from the comparison between in situ and reanalysis data, a future assimilation of glider data in ocean reanalysis data could likely overcome this problem.

As it is known, glider observations are a mix of spatial and temporal variations; however, we treat these observations as purely spatially varying. We are aware that, except at the edges of the Bari–Dubrovnik transect, information on convective cones is provided every 4–5 days. However, based on potential temperature reanalysis data (Fig. 6), we can conclude that the sequence of the in situ cones observed along the first track is likely the same as that observed along the second track.

It is important to highlight that although at the beginning (~24 January) cones form within localized homogeneous water columns of ~300-m depth (Figs. 6c–f), at later time they extend deeper with an inner core denser and colder, therefore influencing the water characteristic during and after the restratification phase.

Experimental studies point out that $D_{\text{cone}} \approx (5.2 \pm 1)\sqrt{R_o^*}\,H$ (Maxworthy and Narimousa 1994) and for our case, $D_{\text{cone}} = 1.7$–2.5 km (with $H = h_{\text{fin}} = 650$ m, $R_o^* = 0.4$, $B_0 = 6 \times 10^{-8}$ m^2 s^{-3}, $f = 10^{-4}$ s^{-1}). However, considering that the radius of the convective region ($r \sim 35$ km) $\gg h_{\text{fin}}$, the interior region is described by the model of Phillips (1966), and a factor of $(r/h)^{1/3}$ should multiply the original estimate of Maxworthy and Narimousa (1994). In this latter case, $D_{\text{cone}} = 6.5$–10 km. The in situ dimension of cone B (13 km) is slightly larger than the predicted one while cone C (10 km) matches the theoretical value (Figs. 2a,b, lower panel). The minimization of the cost function g suggests that cone B and cone C have a diameter of 15 and 11 km, respectively (Fig. 4) and these values are in agreement with the ones provided by the Saunders theory (13 and 10 km, respectively) while the position in space of both centers is 17.5°E for cone B and 17.60°E for cone C.

By 5 February (Fig. 6i), which approximately coincides with the end of the mixing phase (Figs. 2b and 5), the nearly circular shape of the convective site (green isotherms in Fig. 6g) evolves and the meander at its border become more defined. This modified shape recalls the evolution of a convective area constrained by a rim current under the baroclinic instability (Visbeck et al. 1996, their Fig. 2) and, as suggested by the simulation of Visbeck et al. (1996) (among others), baroclinic eddies associated with the growing meanders of the rim current (e.g., Fig. 6i) could explain the spreading/restratification phase. These eddies sweep stratified water into the convective area at the surface arresting the convective process. They demonstrated that the maximum depth h_{fin} at which the mixing is arrested due to the action of these lateral eddies, and the time t_{fin} to reach that depth are

$$h_{\text{fin}} = \delta\frac{(rB_0)^{1/3}}{N}; \quad t_{\text{fin}} = \beta\left(\frac{r^2}{B_0}\right)^{1/3}, \tag{5.2}$$

where $\gamma = 3.9 \pm 0.9$ and $\beta = 12 \pm 3$ are dimensionless constants. For our case ($r = 35$ km, $N = 10^{-3}$ s^{-1}, $B_0 = 6.3\ 10^{-8}$ m^2 s^{-3}) $h_{\text{fin}} \sim 650$ m and $t_{\text{fin}} = 28$ (46) days for $\beta = 9$ (15). Considering that the in situ mixing process lasts approximately 25 days, it is more appropriate to use $t_{\text{fin}} = 28$ days (and not 46). Numerical calculations carried out by A. Lascaratos in 1994 (personal communication with M. Visbeck) shown that an ~80-km diameter convective region takes ~3 weeks for the eddies to be "felt" at the center of the cooling region while, for a region of ~16 km in diameter, time is remarkably smaller. For our study, the convective site has a diameter of ~70 km and $t_{\text{fin}} = 28$ days, which is in agreement with Lascaratos's numerical outputs.

If no eddy action is present, the time required for convection to break through the stratification (t_{break}) is calculated from Eq. (1.2) and equal to ~40 days but, since $t_{\text{fin}} < t_{\text{break}}$, baroclinic eddies seem to play a role in arresting the deepening area. In support of this, a lateral intrusion of warmer water is captured at the western side of the glider transect by in situ measurements (Fig. 2b), and is also simulated by the reanalysis model (Fig. 6j). Specifically, for the in situ cone B, while the inner 14.04°–14.06°C isotherms fall down to greater depths (Fig. 2b), the upper layer ($z < 300$ m) by intruding toward the east pushes the upper left side of the cone B, which bends and folds on itself. Residual traces of cone A are present with the white 14.04°–14.06°C isotherms reaching the depth of $z \sim 650$ m. Therefore, glider potential temperature records resolve the breaking mechanism of cone B and confirm that lateral advection is responsible for breaking the cones and for arresting the deepening area by mixing the upper waters. Unfortunately, reanalysis data are not able to reproduce the breaking mechanism of cone A and cone B. With the restratification phase (Fig. 2c), the water in the upper ~500 m results in colder and denser than the water characteristics of the initial MLD identified with the four patches detected in Fig. 2a ($\rho_\theta = 1029.12$ kg m^{-3}, $\theta = 14.24$°C).

The horizontal length scale of the surface baroclinic eddies at the end of the convective process is assumed to be set by the Rossby radius and scales as $L_{\rho,\text{fin}} = Nh_{\text{fin}}/f = \delta[(rB_0)^{1/3}/f] \sim 6$ km (Visbeck et al. 1996), which is in agreement with what is shown by the reanalysis potential temperature map (Fig. 6i).

After the convective site breaks up and the restratification phase ends (~10 February), atmospheric conditions support the formation of a second mixing event highlighted by the increasing of the vertical velocity w and the modeled buoyancy flux (Figs. 3 and 5c). This time, although only for ~27 h, we collected data during the *convective process*, where the characterization of small convective cells (horizontal and vertical size) that developed along section 5 was possible from the analysis of the glider potential density and temperature (Fig. 2e). According to Legg and Marshall's (1993) results, these colder (warmer) and denser (less dense) cells recorded in the upper 500 m had a horizontal scale on the order of the local Rossby radius of deformation L_ρ (~6 km). Based on these characteristics and on the appearance time, the observed convective cells could probably be associated with the plumes. This finding is in contrast with previous literature review where the plume size is known to be ≤1 km. However, examples reported in literature refer to the Gulf of Lion (GoL), Weddell Sea, Greenland Sea, and Labrador Sea, where the $L_\rho = O(1)$ km and so far, there are no in situ measurements of plume size in the SAP. In regard to this, the authors are

aware that the above hypothesis still needs to be more thoroughly investigated and supported with more information. The work of Margirier et al. (2017) could be a good example to follow.

6. Conclusions

For the first time, glider measurements used to monitor the deep convection phenomena in the SAP revealed a multiscale spatiotemporal variability of the mixing and restratification phases during winter 2018. Within a ~110-km-wide convective region, localized homogeneous water columns form and extend from the near-surface layer down to the intermediate waters. Before the mixing phase ends and when the initial MLD is established, the latter breaks down into cyclonic convective cones due to baroclinic adjustment process. Specifically, this cone formation mechanism occurs when convection does not reach the ocean bottom. Fully developed cones have a maximum radius on the order of $L_\rho \sim 6$ km, a vertical extension of ~600 m, and a lifetime of weeks.

The horizontal density gradient between the convective area and the outside stratified waters supports the formation of surface eddies along the perimeter of the convective site through the baroclinic instability process. These eddies are responsible for arresting the mixing phase and for the initiation of the restratification/spreading process. This mechanism evidences how the atmospheric conditions are not always responsible for restratification/spreading phase occurrence.

The observed dense water formation process (associated to the cyclonic cones formation) which is supported by theoretical arguments and laboratory experiments, to the best of our knowledge, is shown to be different from the one occurring in the GoL and in other ocean sites (e.g., Greenland and Labrador Seas). In these regions, in the case of a no-bottom reaching event, the formation of cyclonic cones is not supported while, when the convective region is fully homogenized down to the ocean bottom, the formation of cyclonic and/or anticyclonic eddies at the periphery of the convective site (usually in a postconvection process) occurs. These long-lived eddies could influence the mixing mechanism occurring during the next winter season.

In light of these findings, more strategic field campaigns will be conducted in the SAP. Specifically, we plan to extend the in situ measurements also to the southern part of the SAP and for a longer period in order to fully investigate the mixing and the spreading/restratification phase along with the detection and characterization of the convective cones.

Acknowledgments. We would like to express our sincere gratitude to Dr. John Marshall (Massachusetts Institute of Technology, Cambridge, Massachusetts) for the fruitful discussions we had and for constructive comments on the manuscript. His scientific suggestions, inputs and encouragement were much appreciated. We also thank Massimo Pacciaroni, Antonio Bussani, and Stefano Kuchler for helping with the glider deployment and piloting; Dr. Vanessa Cardin for providing the E2-M3A data; and Giuseppe Siena for helping with the E2-M3A data collection. This study has been conducted using E.U. Copernicus Marine Service Information (https://doi.org/10.25423/CMCC/MEDSEA_MULTIYEAR_PHY_006_004_E3R1).

REFERENCES

Artegiani, A., R. Azzolini, and E. Salusti, 1989: On the dense water in the Adriatic Sea. *Oceanol. Acta*, **12**, 151–160.

——, E. Paschini, A. Russo, D. Bregant, F. Raicich, and N. Pinardi, 1997: The Adriatic Sea general circulation. Part I: Air–sea interactions and water mass structure. *J. Phys. Oceanogr.*, **27**, 1492–1514, https://doi.org/10.1175/1520-0485(1997)027<1492:TASGCP>2.0.CO;2.

Bensi, M., V. Cardin, and A. Rubino, 2014: Thermohaline variability and mesoscale dynamics observed at the deep-ocean observatory E2M3A in the southern Adriatic Sea. *The Mediterranean Sea: Temporal Variability and Spatial Patterns, Geophys. Monogr.*, Vol. 202, Amer. Geophys. Union, 139–155, https://doi.org/10.1002/9781118847572.ch9.

Blokhina, M. D., and Y. D. Afanasyev, 2003: Baroclinic instability and transient features of mesoscale surface circulation in the Black Sea: Laboratory experiment. *J. Geophys. Res.*, **108**, 3322, https://doi.org/10.1029/2003JC001979.

Bosse, A., P. Testor, L. Mortier, L. Prieur, V. Taillandier, F. d'Ortenzio, and L. Coppola, 2015: Spreading of Levantine Intermediate Waters by submesoscale coherent vortices in the northwestern Mediterranean Sea as observed with gliders. *J. Geophys. Res. Oceans*, **120**, 1599–1622, https://doi.org/10.1002/2014JC010263.

——, and Coauthors, 2016: Scales and dynamics of submesoscale coherent vortices formed by deep convection in the northwestern Mediterranean Sea. *J. Geophys. Res. Oceans*, **121**, 7716–7742, https://doi.org/10.1002/2016JC012144.

Buljan, M., and M. Zore-Armanda, 1976: Oceanographical properties of the Adriatic Sea. *Oceanogr. Mar. Biol.*, **14**, 11–98.

Cushman-Roisin, B., M. Gacic, P. M. Poulain, and A. Artegiani, Eds., 2001: *Physical Oceanography of the Adriatic Sea: Past, Present and Future*. Springer, 318 pp.

Damien, P. P., A. Bosse, P. Testor, P. Marsaleix, and C. Estournel, 2017: Modeling postconvective submesoscale coherent vortices in the northwestern Mediterranean Sea. *J. Geophys. Res. Oceans*, **122**, 9937–9961, https://doi.org/10.1002/2016JC012114.

Deardorff, J. W., 1985: Mixed-layer entrainment: A review. *Proc. Seventh Symp. on Atmospheric Turbulence and Diffusion*, Boulder, CO, Amer. Meteor. Soc., 39–42.

Du Plessis, M., S. Swart, I. J. Ansorge, and A. Mahadevan, 2017: Submesoscale processes promote seasonal restratification in the Subantarctic Ocean. *J. Geophys. Res. Oceans*, **122**, 2960–2975, https://doi.org/10.1002/2016JC012494.

Eady, E. T., 1949: Long waves and cyclone waves. *Tellus*, **1**, 33–52, https://doi.org/10.3402/tellusa.v1i3.8507.

Elliott, B. A., and T. B. Sanford, 1986: The subthermocline lens D1. Part II: Kinematics and dynamics. *J. Phys. Oceanogr.*, **16**, 549–561, https://doi.org/10.1175/1520-0485(1986)016<0549:TSLDPI>2.0.CO;2.

Fernando, H. J., R. R. Chen, and D. L. Boyer, 1991: Effects of rotation on convective turbulence. *J. Fluid Mech.*, **228**, 513–547, https://doi.org/10.1017/S002211209100280X.

Gačić, M., G. Civitarese, S. Miserocchi, V. Cardin, A. Crise, and E. Mauri, 2002: The open-ocean convection in the Southern Adriatic: A controlling mechanism of the spring phytoplankton

bloom. *Cont. Shelf Res.*, **22**, 1897–1908, https://doi.org/10.1016/S0278-4343(02)00050-X.

Gascard, J.-C., and R. A. Clarke, 1983: The formation of Labrador Sea Water. Part 2: Mesoscale and smaller scale processes. *J. Phys. Oceanogr.*, **13**, 1779–1797, https://doi.org/10.1175/1520-0485(1983)013<1779:TFOLSW>2.0.CO;2.

Gordon, A. L., 1982: Weddel deep water variability. *J. Mar. Res.*, **40**, 199–217.

Grilli, F., and N. Pinardi, 1998: The computation of Rossby radii of deformation for the Mediterranean Sea. *MTP News*, No. 6, 4.

Helfrich, K. R., 1994: Thermals with background rotation and stratification. *J. Fluid Mech.*, **259**, 265–280, https://doi.org/10.1017/S0022112094000121.

Houpert, L., and Coauthors, 2016: Observations of open-ocean deep convection in the northwestern Mediterranean Sea: Seasonal and interannual variability of mixing and deep water masses for the 2007-2013 period. *J. Geophys. Res. Oceans*, **121**, 8139–8171, https://doi.org/10.1002/2016JC011857.

Ivey, G. N., J. R. Taylor, and M. J. Coates, 1995: Convectively driven mixed layer growth in a rotating, stratified fluid. *Deep-Sea Res. I*, **42**, 331–349, https://doi.org/10.1016/0967-0637(94)00039-U.

Jones, H., and J. Marshall, 1993: Convection with rotation in a neutral ocean: A study of open-ocean deep convection. *J. Phys. Oceanogr.*, **23**, 1009–1039, https://doi.org/10.1175/1520-0485(1993)023<1009:CWRIAN>2.0.CO;2.

——, and ——, 1997: Restratification after deep convection. *J. Phys. Oceanogr.*, **27**, 2276–2287, https://doi.org/10.1175/1520-0485(1997)027<2276:RADC>2.0.CO;2.

Killworth, P. D., 1976: The mixing and spreading phases of MEDOC. I. *Prog. Oceanogr.*, **7**, 59–90, https://doi.org/10.1016/0079-6611(76)90005-7.

——, 1979: On "chimney" formations in the ocean. *J. Phys. Oceanogr.*, **9**, 531–554, https://doi.org/10.1175/1520-0485(1979)009<0531:OFITO>2.0.CO;2.

Kokkini, Z., E. Mauri, R. Gerin, P. M. Poulain, S. Simoncelli, and G. Notarstefano, 2020: On the salinity structure in the South Adriatic as derived from float and glider observations in 2013–2016. *Deep-Sea Res. II*, **171**, 104625, https://doi.org/10.1016/j.dsr2.2019.07.013.

Kovačević, V., M. Gacić, and P. M. Poulain, 1999: Eulerian current measurements in the Strait of Otranto and in the Southern Adriatic. *J. Mar. Syst.*, **20**, 255–278, https://doi.org/10.1016/S0924-7963(98)00086-4.

Leaman, K. D., and F. A. Schott, 1991: Hydrographic structure of the convection regime in the Gulf of Lions: Winter 1987. *J. Phys. Oceanogr.*, **21**, 575–598, https://doi.org/10.1175/1520-0485(1991)021<0575:HSOTCR>2.0.CO;2.

Legg, S., and J. Marshall, 1993: A heton model of the spreading phase of open-ocean deep convection. *J. Phys. Oceanogr.*, **23**, 1040–1056, https://doi.org/10.1175/1520-0485(1993)023<1040:AHMOTS>2.0.CO;2.

——, J. Mc Williams, and J. Gao, 1998: Localization of deep ocean convection by a geostrophic eddy. *J. Phys. Oceanogr.*, **28**, 944–970, https://doi.org/10.1175/1520-0485(1998)028<0944:LODOCB>2.0.CO;2.

Lilly, J. M., and P. B. Rhines, 2002: Coherent eddies in the Labrador Sea observed from a mooring. *J. Phys. Oceanogr.*, **32**, 585–598, https://doi.org/10.1175/1520-0485(2002)032<0585:CEITLS>2.0.CO;2.

——, ——, M. Visbeck, R. Davis, J. R. Lazier, F. Schott, and D. Farmer, 1999: Observing deep convection in the Labrador Sea during winter 1994/95. *J. Phys. Oceanogr.*, **29**, 2065–2098, https://doi.org/10.1175/1520-0485(1999)029<2065:ODCITL>2.0.CO;2.

Malanotte-Rizzoli, P., and Coauthors, 1997: A synthesis of the Ionian Sea hydrography, circulation and water mass pathways during POEM- Phase I. *Prog. Oceanogr.*, **39**, 153–204, https://doi.org/10.1016/S0079-6611(97)00013-X.

Manca, B., and D. Bregant, 1998: Dense water formation and circulation in the Southern Adriatic Sea during winter 1996. *Rapp. P.-V. Reun. Comm. Int. Explor. Sci. Mer Mediterr.*, **35**, 176–177.

——, and A. Giorgetti, 1998: Thermohaline properties and circulation patterns in the Southern Adriatic Sea from May 1995 to 12 February 1996. *Atti del 12° Congresso dell'Associazione Italiana di Oceanologia e Limnologia*, Vol. II, M. Piccazzo, Ed., Associazione Italiana di Oceanologia e Limnologia, 399–414.

Manca, B. B., V. Kovaĉević, M. Gaĉić, and D. Viezzoli, 2002: Dense water formation in the Southern Adriatic Sea and spreading into the Ionian Sea in the period 1997–1999. *J. Mar. Syst.*, **33–34**, 133–154, https://doi.org/10.1016/S0924-7963(02)00056-8.

Mantziafou, A., and A. Lascaratos, 2004: An eddy resolving numerical study of the general circulation and deep-water formation in the Adriatic Sea. *Deep-Sea Res. I*, **51**, 921–952, https://doi.org/10.1016/j.dsr.2004.03.006.

——, and ——, 2008: Deep-water formation in the Adriatic Sea: Interannual simulations for the years 1979–1999. *Deep-Sea Res. I*, **55**, 1403–1427, https://doi.org/10.1016/j.dsr.2008.06.005.

Margirier, F., and Coauthors, 2017: Characterization of convective plumes associated with oceanic deep convection in the northwestern Mediterranean from high-resolution in situ data collected by gliders. *J. Geophys. Res. Oceans*, **122**, 9814–9826, https://doi.org/10.1002/2016JC012633.

Marshall, J., and F. Schott, 1999: Open-ocean convection, observations, theory, and models. *Rev. Geophys.*, **37**, 1–64, https://doi.org/10.1029/98RG02739.

——, J. A. Whitehead, and T. Yates, 1994: Laboratory and numerical experiments in oceanic convection. *Ocean Processes in Climate Dynamics: Global and Mediterranean Examples*, P. Malanotte-Rizzoli and A. Robinson, Eds., Springer, 173–201.

Maxworthy, T., and S. Narimousa, 1992: Rotating convection. *Interactive Dynamics of Convection and Solidification*, S. H. Davis et al., Eds., NATO Science Series E, Vol. 219, Springer, 261–263.

——, and ——, 1994: Unsteady, turbulent convection into a homogeneous, rotating fluid, with oceanographic applications. *J. Phys. Oceanogr.*, **24**, 865–887, https://doi.org/10.1175/1520-0485(1994)024<0865:UTCIAH>2.0.CO;2.

Merckelbach, L., D. Smeed, and G. Griffiths, 2010: Vertical water velocities from underwater gliders. *J. Atmos. Oceanic Technol.*, **27**, 547–563, https://doi.org/10.1175/2009JTECHO710.1.

Mertens, C., 2000: Open-ocean convection in the Labrador and Greenland Seas: Plume scales and interannual variability. Ph.D. dissertation, Faculty of Mathematics and Natural Sciences, Kiel University, 134 pp.

——, and F. Schott, 1998: Interannual variability of deep-water formation in the northwestern Mediterranean. *J. Phys. Oceanogr.*, **28**, 1410–1424, https://doi.org/10.1175/1520-0485(1998)028<1410:IVODWF>2.0.CO;2.

Nardelli, B. B., and E. Salusti, 2000: On dense water formation criteria and their application to the Mediterranean Sea. *Deep-Sea Res. I*, **47**, 193–221, https://doi.org/10.1016/S0967-0637(99)00054-0.

Oddo, P., N. Pinardi, and M. Zavatarelli, 2005: A numerical study of the interannual variability of the Adriatic Sea (2000–2002). *Sci. Total Environ.*, **353**, 39–56, https://doi.org/10.1016/j.scitotenv.2005.09.061.

Ovchinnikov, I. M., V. I. Zats, V. G. Krivosheya, and A. I. Udodov, 1985: Formation of deep Eastern Mediterranean waters in the Adriatic Sea. *Oceanology*, **25**, 704–707.

Penven, P., I. Halo, S. Pous, and L. Marie, 2014: Cyclogeostrophic balance in the Mozambique Channel. *J. Geophys. Res. Oceans*, **119**, 1054–1067, https://doi.org/10.1002/2013JC009528.

Phillips, O. M., 1966: On turbulent convection currents and the circulation of the Red Sea. *Deep-Sea Res. Oceanogr. Abstr.*, 13, 1149–1160, https://doi.org/10.1016/0011-7471(66)90706-6.

Pollak, M. I., 1951: The sources of the deep water in the eastern Mediterranean. *J. Mar. Res.*, **10**, 128–152.

Poulain, P.-M., 2001: Adriatic Sea surface circulation as derived from drifter data between 1990 and 1999. *J. Mar. Syst.*, **29**, 3–32, https://doi.org/10.1016/S0924-7963(01)00007-0.

——, and B. Cushman-Roisin, 2001: Circulation. *Physical Oceanography of the Adriatic Sea Past, Present and Future*, B. Cushman-Roisin et al., Eds., Springer, 312 pp.

——, M. Menna, and E. Mauri, 2012: Surface geostrophic circulation of the Mediterranean Sea derived from drifter and satellite altimeter data. *J. Phys. Oceanogr.*, **42**, 973–990, https://doi.org/10.1175/JPO-D-11-0159.1.

Querin, S., G. Cossarini, and C. Solidoro, 2013: Simulating the formation and fate of dense water in a midlatitude marginal sea during normal and warm winter conditions. *J. Geophys. Res. Oceans*, **118**, 885–900, https://doi.org/10.1002/jgrc.20092.

Saunders, P. M., 1973: The instability of a baroclinic vortex. *J. Phys. Oceanogr.*, **3**, 61–65, https://doi.org/10.1175/1520-0485(1973)003<0061:TIOABV>2.0.CO;2.

Schlitzer, R., W. Roether, H. Oster, H. G. Junghans, M. Hausmann, and A. Michelato, 1991: Chlorofluoromethane and oxygen in the Eastern Mediterranean. *Deep-Sea Res.*, **38**, 1531–1551, https://doi.org/10.1016/0198-0149(91)90088-W.

Schott, F., and K. D. Leaman, 1991: Observations with moored acoustic Doppler current profilers in the convection regime in the Golfe du Lion. *J. Phys. Oceanogr.*, **21**, 558–574, https://doi.org/10.1175/1520-0485(1991)021<0558:OWMADC>2.0.CO;2.

——, M. Visbeck, and J. Fischer, 1993: Observations of vertical currents and convection in the central Greenland Sea during the winter of 1988–1989. *J. Geophys. Res.*, **98**, 14 401–14 421, https://doi.org/10.1029/93JC00658.

——, ——, U. Send, J. Fischer, L. Stramma, and Y. Desaubies, 1996: Observations of deep convection in the Gulf of Lions, northern Mediterranean, during the winter of 1991/92. *J. Phys. Oceanogr.*, **26**, 505–524, https://doi.org/10.1175/1520-0485(1996)026<0505:OODCIT>2.0.CO;2.

Stommel, H., 1972: Deep winter-time convection in the western Mediterranean Sea. *Studies in Physical Oceanography: A Tribute to Georg Wust on his 80th Birthday*, A. L. Gordon, Ed., Vol. 2, Gordon and Breach, 207–218.

——, A. Voorhis, and D. Webb, 1971: Submarine clouds in the deep ocean: Surface cooling during late winter in the northwestern Mediterranean Sea causes large masses of water to sink to great depths. *Amer. Sci.*, **59**, 716–722.

Swart, S., S. J. Thomalla, and P. M. S. Monteiro, 2015: The seasonal cycle of mixed layer dynamics and phytoplankton biomass in the Sub-Antarctic Zone: A high-resolution glider experiment. *J. Mar. Syst.*, **147**, 103–115, https://doi.org/10.1016/j.jmarsys.2014.06.002.

Testor, P., and Coauthors, 2019: OceanGliders: A component of the integrated GOOS. *Front. Mar. Sci.*, **6**, 422, https://doi.org/10.3389/fmars.2019.00422.

Thomalla, S. J., M. Racault, S. Swart, and P. M. S. Monteiro, 2015: High-resolution view of the spring bloom initiation and net community production in the Subantarctic Southern Ocean using glider data. *ICES J. Mar. Sci.*, **72**, 1999–2020, https://doi.org/10.1093/icesjms/fsv105.

Todd, R. E., D. L. Rudnick, and R. E. Davis, 2009: Monitoring the greater San Pedro Bay region using autonomous underwater gliders during fall of 2006. *J. Geophys. Res.*, **114**, C06001, https://doi.org/10.1029/2008JC005086.

Turner, J. S., 1973: *Buoyancy Effects in Fluids*. Cambridge University Press, 368 pp.

Visbeck, M., J. Marshall, and H. Jones, 1996: Dynamics of isolated convective regions in the ocean. *J. Phys. Oceanogr.*, **26**, 1721–1734, https://doi.org/10.1175/1520-0485(1996)026<1721:DOICRI>2.0.CO;2.

Whitehead, J. A., J. Marshall, and G. E. Hufford, 1996: Localized convection in rotating stratified fluid. *J. Geophys. Res.*, **101**, 25 705–25 721, https://doi.org/10.1029/96JC02322.

Wüst, G., 1961: On the vertical circulation of the Mediterranean Sea. *J. Geophys. Res.*, **66**, 3261–3271, https://doi.org/10.1029/JZ066i010p03261.